Title

A comprehensive Drosophila resource to identify key functional interactions between SARS-CoV-2 factors and host proteins.

Journal

Cell Reports, 42(8)

Authors

Guichard, Annabel

Lu, Shenzhao

Kanca, Oguz

et al.

Publication Date

2023-08-29

DOI

10.1016/j.celrep.2023.112842

Peer reviewed

Published in final edited form as:

Cell Rep. 2023 August 29; 42(8): 112842. doi:10.1016/j.celrep.2023.112842.

A comprehensive *Drosophila* resource to identify key functional interactions between SARS-CoV-2 factors and host proteins

Annabel Guichard[1,14], **Shenzhao Lu**[2,3,14], **Oguz Kanca**[2,3,14], **Daniel Bressan**[1,4], **Yan Huang**[2,3], **Mengqi Ma**[2,3], **Sara Sanz Juste**[1,5,6], **Jonathan C. Andrews**[2,3], **Kristy L. Jay**[2,3], **Marketta Sneider**[1], **Ruth Schwartz**[1], **Mei-Chu Huang**[2,3], **Danqing Bei**[2,3], **Hongling Pan**[2,3], **Liwen Ma**[2,3], **Wen-Wen Lin**[2,3], **Ankush Auradkar**[1], **Pranjali Bhagwat**[2,3], **Soo Park**[7], **Kenneth H. Wan**[7], **Takashi Ohsako**[8], **Toshiyuki Takano-Shimizu**[9], **Susan E. Celniker**[7], **Michael F. Wangler**[2,3,10], **Shinya Yamamoto**[2,3,11,12,*], **Hugo J. Bellen**[2,3,11,15,*], **Ethan Bier**[1,13,*]

[1]Section of Cell and Developmental Biology, University of California, San Diego (UCSD), La Jolla, CA 92093, USA

[2]Department of Molecular and Human Genetics, Baylor College of Medicine, Houston, TX 77030, USA

[3]Jan and Dan Duncan Neurological Research Institute, Texas Children's Hospital, Houston, TX 77030, USA

[4]Instituto de Ciências Biomédicas (ICB), Universidade Federal do Rio de Janeiro, Rio de Janeiro, Rio de Janeiro 21941-902, Brazil

[5]Department of Epigenetics & Molecular Carcinogenesis at MD Anderson, The University of Texas MD Anderson Cancer Center, Houston, TX 77054, USA

[6]Center for Cancer Epigenetics, MD Anderson Cancer Center, Houston, TX, USA

[7]Biological Systems and Engineering, Lawrence Berkeley National Laboratory, Berkeley, CA 94720, USA

[8]Advanced Technology Center, Kyoto Institute of Technology, Kyoto 606-8585, Japan

[9]Kyoto Drosophila Stock Center and Faculty of Applied Biology, Kyoto Institute of Technology, Kyoto 616-8354, Japan

[*]Correspondence: yamamoto@bcm.edu (S.Y.), hbellen@bcm.edu (H.J.B.), ebier@ucsd.edu (E.B.).

AUTHOR CONTRIBUTIONS

H.J.B., E.B., and S.Y. conceived and designed the project. A.G., S.L., and O.K. designed and conducted and analyzed most experiments. D.B., Y.H., M.M., S.S.J., M.S., and R.S. performed and analyzed some fly experiments. M.-C.H., S.P., and K.H.W. performed cloning and coordination of the human cDNAs. D.B., H.P., L.M., W.-W.L., and T.O. contributed to injection and stock establishment of transgenic and mutant strains. S.Y., H.J.B., S.E.C., T.T.-S., and O.K. supervised the transgenic and mutant strain generation. J.C.A., K.L.J., M.S., R.S., A.A., and P.B. generated a subset of reagents and performed some fly experiments. M.F.W. designed part of the project and supervised some fly experiments. J.C.A., Y.H., M.S., and M.M. edited the manuscript. A.G., S.L., O.K., S.Y., H.J.B., and E.B. wrote and revised the manuscript.

SUPPLEMENTAL INFORMATION

Supplemental information can be found online at https://doi.org/10.1016/j.celrep.2023.112842.

DECLARATION OF INTERESTS

E.B. has equity interests in Synbal Inc., a company that may potentially benefit from the research results. E.B. also serves on the Board of Directors and Scientific Advisory Board of Synbal. The terms of this arrangement have been reviewed and approved by the University of California, San Diego in accordance with its conflict-of-interest policies.

[10]Texas Children's Hospital, Houston, TX 77030, USA

[11]Department of Neuroscience, Baylor College of Medicine, Houston, TX 77030, USA

[12]Development, Disease Models & Therapeutics Graduate Program, Baylor College of Medicine, Houston, TX 77030, USA

[13]Tata Institute for Genetics and Society - UCSD, La Jolla, CA 92093, USA

[14]These authors contributed equally

[15]Lead contact

SUMMARY

Development of effective therapies against SARS-CoV-2 infections relies on mechanistic knowledge of virus-host interface. Abundant physical interactions between viral and host proteins have been identified, but few have been functionally characterized. Harnessing the power of fly genetics, we develop a comprehensive *Drosophila* COVID-19 resource (DCR) consisting of publicly available strains for conditional tissue-specific expression of all SARS-CoV-2 encoded proteins, UAS-human cDNA transgenic lines encoding established host-viral interacting factors, and GAL4 insertion lines disrupting fly homologs of SARS-CoV-2 human interacting proteins. We demonstrate the utility of the DCR to functionally assess SARS-CoV-2 genes and candidate human binding partners. We show that NSP8 engages in strong genetic interactions with several human candidates, most prominently with the ATE1 arginyltransferase to induce actin arginylation and cytoskeletal disorganization, and that two ATE1 inhibitors can reverse NSP8 phenotypes. The DCR enables parallel global-scale functional analysis of SARS-CoV-2 components in a prime genetic model system.

Graphical abstract

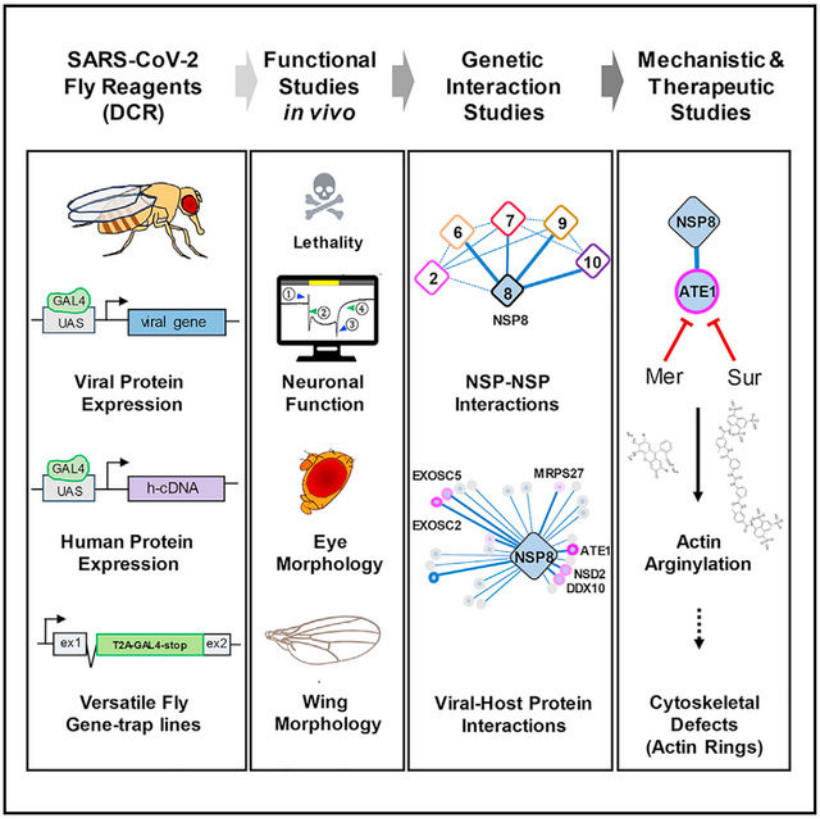

In brief

Guichard et al. develop *Drosophila* tools for conditional tissue-specific expression of individual SARS-CoV-2 factors and candidate human binding partners, as well as functional characterization of their fly orthologs. This resource is shared with the scientific community to promote analysis of *in vivo* interactions between viral and host factors.

INTRODUCTION

The current COVID-19 pandemic crisis has inflicted catastrophic global impacts on public health and the economy.[1–3] Moreover, recurrent waves of infection have produced mutations altering viral infectivity and/or pathogenicity.[4] SARS-CoV-2 can also cause a myriad of persisting symptoms often referred to as long-COVID or post-acute sequelae of COVID (PASC), which may pose a continuing public health burden in the future. Gaining mechanistic knowledge of SARS-CoV-2 interaction with host processes at the molecular, cellular, and tissue/organ levels is important for developing new therapeutic strategies to meet these current and future challenges.

SARS-CoV-2 is an enveloped, positive-sense, single-stranded RNA virus, with a 29 kb genome encoding seven open reading frames (ORF1–7) and 29 proteins. The first event following cell entry is the direct translation of ORF1ab into a polyprotein, which is self-processed to liberate 16 separate non-structural proteins (NSP1–16). The early-acting NSP proteins (NSPs) encoded by Orf1a engage in a variety of interactions with host cellular

processes as well as the viral replicative machinery encoded by ORF1b.[5,6] In addition, proteomic studies have identified a wealth of physical interactions between viral and host proteins.[7–12] The functional significance of most of these interactions, however, remains to be determined.

Here we report the development of a comprehensive *Drosophila* COVID-19 resource (DCR), an extensive toolkit to systematically probe the functional interactions between viral and host proteins using the fruit fly *Drosophila melanogaster* as an *in vivo* discovery system. The design of these reagents and the strategies employed parallel previous studies delineating viral protein functions in flies. For example, one study relating to the influenza virus[13] and another to the Zika virus[14–16] led to insights into the molecular functions of viral factors. In the former study, we identified and characterized a novel Hedgehog (Hh) pathway modulating activity associated with the influenza protein NS1.[13] In a second study, we documented that the Zika virus protein NS4A acts through the host ANKLE2 protein to disrupt neural development and induce microcephaly.[16–20] *Drosophila* has also been employed to study a variety of pathogenic factors[17–19] including proteins relevant to SARS-CoV-2 infection,[20–22] such as ACE2-related receptors,[23] ORF6a,[20] and NSP6.[24] These compelling *Drosophila*-based mechanistic discoveries prompted us to generate the DCR, a comprehensive collection of publicly available reagents to accelerate COVID research.

The DCR leverages the full power of advanced *Drosophila* genetics to enable parallel exploration of basic biological features associated with SARS-CoV-2 infection (Figure 1). We first created transgenic lines encoding each viral protein to produce characteristic phenotypes. In parallel, based on data from a previous proteomics study which identified 332 human proteins physically binding to viral factors,[9] we created 234 transgenic strains carrying full-length human cDNAs. Co-expression of these human proteins with the corresponding binding viral proteins can reveal whether the human and viral proteins functionally interact. We also created a library of 313 mutant stocks of the fly homologs of the human genes/proteins interactors by inserting T2A-GAL4 or Kozak-GAL4 encoding cassettes.[25–27] This comprehensive set of GAL4 insertional strains can be employed to determine loss-of-function (L-o-F) phenotypes associated with the targeted genes and their expression patterns or to express human interacting factors in patterns mimicking those of their fly homologs for “humanization” assays. The flexible and integrated features of the DCR permit rapid identification of phenotypes associated with expression of SARS-CoV-2 proteins in specific cell types, tissues, or organs and provide the genetic leverage to perform in-depth analysis of fly phenotypes to establish the mechanistic basis for virus-host interactions (Figure 1). We provide several proof-of-concept examples for employing the DCR toolbox to uncover new functions of SARS-CoV-2 proteins *in vivo*, highlighting the discovery of a novel interaction between the viral NSP8 protein human ATE1 arginyltransferase, which modifies actin and alters the cellular cytoskeleton.

RESULTS

We systematically evaluated the activities of SARS-CoV-2 factors and their interactions with human candidate partners in *Drosophila* (Figure 1) by creating three classes of reagents.

UAS-SARS-CoV-2 transgenic lines

The SARS-CoV-2 genome encodes 16 non-structural proteins (NSP1–16), four structural proteins (spike [S], envelope [E], membrane [M], and nucleocapsid [N]), and nine putative accessory factors (ORF3a, ORF3b, ORF6, ORF7a, ORF7b, ORF8, ORF9b, ORF9c, and ORF10)[9] (Figure 2A). We obtained SARS-CoV-2 ORF plasmids,[28] encoding 28 of the 29 viral proteins. We used these constructs to generate a collection of transgenic lines carrying upstream activator sequence (UAS)-driven constructs that permit cell- or tissue-specific expression in the presence of the GAL4 *trans*-activator protein.[29] Since NSP11 was not included in the publicly available SARS-CoV-2 plasmid collection, we subcloned it separately. The sequence of the proteins is based on the "2019-nCoV" reference strain (GenBank: MN908947).[30] We initially generated two versions for each viral transgene, one followed by a stop codon (closed clones) and another lacking the stop codon (open clones), into pGW-HA.attB[31] (Figure 2B). A closed clone will produce an untagged protein upon expression of GAL4, while an open clone will encode a protein with a C-terminal 33HA (hemagglutinin) tag. Non-tagged proteins are likely to behave more similarly to the endogenous viral proteins while tagged proteins would permit protein quantification, subcellular localization analysis, and identification of host interacting proteins via co-immuno-precipitation.[32] The UAS-cDNA expression cassettes were inserted into the same genomic locus on the second chromosome (VK37 docking site) via φC31-mediated transgenesis[33] (Table S1). We also generated *UAS-Kozak-NSP* lines with an optimized Kozak sequence inserted before the viral cDNA for the first ten early-acting NSPs (NSP1–10). This modification leads to a significant increase in translational efficiency and concomitant potency of the viral factors (Figures 2B and S3).

UAS-human cDNA lines

A set of 332 human proteins physically interacting with individual SARS-CoV-2 proteins has been previously identified.[9] We obtained full-length human cDNAs from public or commercial sources encoding 261 of these proteins, subcloned them into the pGW-HA.attB or pUASg-HA.attB UAS plasmids,[31] and generated fly lines carrying UAS-human cDNA constructs via φC31-mediated transgenesis[33] (Figure 2C and Table S2). These human SARS-CoV-2-interacting proteins have been implicated in diverse biological processes that are potentially impacted by SARS-CoV-2 infection, such as endoplasmic reticulum (ER) homeostasis and stress response, protein glycosylation, mitochondrial function, centrosome and cytoskeletal dynamics, vesicular trafficking, and exosome formation.[9] Because components of such core cellular pathways are highly conserved, they are readily amenable to functional studies in *Drosophila*. Indeed, 90% of the identified human proteins that interact with SARS-CoV-2 viral proteins have ortholog candidates in flies.[21] To date we have created 242 UAS-human cDNA stocks, and 19 more lines are currently under construction (Table S2).

T2A-GAL4 and Kozak-GAL4 insertions in fly ortholog candidates of human interactors

An important aspect of our assessment of interactions between SARS-CoV-2 factors and candidate human proteins is to establish the function of their *Drosophila* ortholog candidates. The 332 human genes are predicted to be homologous to 407fly genes (using

the ortholog predictor DIOPT, with scores ≥3).[34] There are more fly ortholog candidates than human genes because some human genes have several fly orthologs. We inserted an artificial exon composed of *attP-FRT-SpliceAcceptor*(*SA*)-*T2A-GAL4-polyA- 3XP3EGFP-polyA-FRT-attP* into coding introns (introns that separate two coding exons) for 177 out of 186 genes that have a sufficiently large coding intron using CRISPR-mediated homology-directed repair (HDR) or by recombinase-mediated cassette exchange (RMCE) of existing MiMIC lines[25,27,35–37] (Figure 2D). These inserts typically create strong L-o-F alleles of the targeted gene. Additionally, such alleles can be employed to determine the expression patterns of targeted genes and establish whether the human and fly genes have conserved molecular functions through rescue experiments.[38–47] We targeted another 136 out of 210 genes that do not have a suitable coding intron employing a knockout/knockin approach using *Kozak-GAL4-FRT-3XP3EGFP-FRT* cassette to replace the coding sequence of the gene via HDR.[26] Additionally, in three cases where the only available intron is in the 5′ UTR, we opted to replace the coding region with a *SA-KozakGAL4* cassette[26] (Figure 2D). These alleles permit rescue strategies similar to those employed with the T2A-GAL4 insertions. In summary, we generated GAL4 alleles for 313 fly gene ortholog candidates corresponding to 216 of the 332 human genes that encode for SARS-CoV-2 interactors (Table S3).

Thirteen out of 29 SARS-CoV-2 factors cause lethality when ubiquitously expressed

As a first step in assessing the functions of individual SARS-CoV-2 proteins, we determined whether ubiquitous expression of these viral factors causes lethality (Figure 1). We selected three ubiquitous drivers: *Actin*(*Act*)-*GAL4*, *Tubulin*(*Tub*)-*GAL4* (strong drivers), and *daughterless*(*da*)-*GAL4* (milder driver). Among the 29 SARS-CoV-2 proteins tested expressed by the non-Kozak insertions, 13 (NSP1, NSP3, NSP5, NSP6, NSP13, NSP14, NSP15, E, M, ORF3a, ORF6, ORF7a, and ORF7b) caused lethality using at least one driver and seven proteins caused lethality with all three (Figures 3A and 3B), suggesting disruption of an essential activity. The stages of lethality produced by all transgenes with *da-GAL4* are listed in Table S4. We also systematically compared the severity of phenotypes caused by overexpression of the native versus HA-tagged transgenes (Figure S3). These experiments revealed that 16 genes (55%) caused comparable lethality whether tagged or not, while 11 genes (38%) generated more severe phenotypes when HA tagged (Figure 3C). Since previous studies have demonstrated that HA tags do not typically alter protein levels, distribution, or activity,[31] the basis for these differences will need further examination.

Photoreceptor-specific expression of SARS-CoV-2 proteins alter neural function

Numerous reports have documented entry of the SARS-CoV-2 virus into brains of infected patients,[48] and approximately 70% of hospitalized COVID-19 patients present neurological symptoms.[49] We therefore characterized the effects of a subset of SARS-CoV-2 proteins in the nervous system by overexpressing individual viral proteins in photoreceptor neurons (using *Rhodopsin1*(*Rh1*)-*GAL4*) and performed electroretinogram (ERG) recordings on adult flies (Figure S1A). Of the seven viral transgenes that cause lethality with all three GAL4 lines, six caused ERG defects (NSP1, NSP5, NSP13, NSP15, ORF3a, and ORF6; Figure S1B). Among them, NSP5 severely altered ERGs, including a marked reduction in on-transient, off-transient (both indicating defects in neuronal connection or synaptic

transmission), and depolarization (reflecting defects in phototransduction), at 10 days post eclosion (Figure S1C). The other five proteins displayed more modest and age-dependent ERG defects. In these lines, reduction of on-transient, off-transient, and/or depolarization defects became obvious only by 20 days post eclosion (Figures S1B and S1D–S1F). These data suggest that SARS-CoV-2 proteins disrupt multiple neurological processes, several of which worsen with age.

An allelic variant in *ORF3a* reduces protein activity

As is typical for RNA viruses, the genome of SARS-CoV-2 has evolved since its original documentation.[50] Determining which of the emerging mutation(s) alter pathogenicity represents a significant challenge. For example, the accessory protein ORF3a encodes a viroporin that promotes apoptosis and viral release.[51–55] The p.Q57H variant in ORF3a was initially proposed to be associated with elevated infectivity and mortality.[56,57] However, another study reported that the activity of ORF3a$^{p.Q57H}$ is comparable to that of the reference ORF3a allele.[58] We compared the relative activities of these two alleles by generating a strain of flies carrying the *UAS-ORF3a^{H57}* allele inserted into the same genomic site as the reference *UAS-ORF3a^{Q57}* allele. Expression of reference ORF3a using a variety of GAL4 drivers caused lethality at the embryonic stage (Figures S2A and S2B). Expression of ORF3a$^{p.Q57H}$ in the developing wing (*nubbin-GAL4*), pan-neuronally (e*lav-GAL4*), or ubiquitously (*da-GAL4*) also caused lethality, but at later developmental stages. When expressed in developing wings, ORF3a$^{p.Q57H}$ causes significantly milder phenotype than that produced by the reference ORF3a (Figures S2C and S2D). Consistently, expression of ORF3a$^{p.Q57H}$ in the developing eye and head using the *ey-GAL4* driver caused milder morphological defects than the reference protein (Figure S2E). This difference was not associated with reduced protein levels (Figure S2F), indicating that the p.Q57H variant is less toxic than the reference ORF3a protein.

Expression of NSP1–10 in developing wings produces distinct phenotypes

The *Drosophila* wing can be employed as a sensitive *in vivo* system for assessing biological activities of candidate virulence factors based on overexpression phenotypes and genetic epistasis analyses.[13,59–61] The wing consists of five major longitudinal veins (L1–L5) (Figure 4A). Defects in major developmental signaling pathways result in characteristic wing phenotypes.[59] For example, loss of epidermal growth factor receptor/mitogen-activated protein kinase (EGFR/MAPK) signaling causes vein truncations and small elongated wings,[62,63] reduced bone morphogenetic protein (BMP) signaling decreases L2-L3 and L4-L5 vein spacing,[64,65] loss of Hh signaling reduces L3-L4 vein spacing,[66,67] and reduced Notch signaling leads to thickened veins and gaps along the wing margin[68] (Figure 4A). Hence, wing phenotypes induced by viral factors can provide clues about which signaling pathways they impact. For this analysis, we employed the UAS-Kozak-NSP lines to produce the NSP1–10 proteins at higher expression levels (Figures S3A–S3C).

We exploited a wing-specific GAL4 driver (MS1096,[69] referred to as wingGAL4 hereafter) to express individual NSP proteins throughout the developing wing pouch, with higher levels in the dorsal surface (Figure 4B). Expression of all but one of the NSPs tested generated reproducible, penetrant, and distinctive phenotypes that depended on transgene

expression levels (Figure 4C). These phenotypes include small misshapen wings with blisters suggesting loss of cell adhesion (NSP1 and NSP5), small curled wings suggesting reduced growth (NSP2, NSP3, and NSP6), truncated veins reflective of reduced EGFR/MAPK signaling (NSP3 and NSP6), thickened L3 and L5 veins typical of impaired Notch signaling (NSP4, NSP6, and NSP10), reduced L3-L4 spacing reminiscent of reduced Hh signaling (NSP5), approximation of the L2 and L3 veins suggesting decreased BMP signaling (NSP6 and NSP8), and ectopic veins (NSP9) as seen in *net*[70] or *plexus*[71] mutants. We find that NSP1 and NSP3–5 have the strongest effects (expression of these factors needs to be reduced to obtain viable flies), NSP6 and NSP8 have intermediate strength, while NSP2, NSP9, and NSP10 have weak activity. Only NSP7 failed to produce any phenotype. These relative phenotype severities in the wing parallel observations from the lethality analyses (Figures 3 and Figure S3A).

Because phenotypes from overexpressing NSP3 and NSP6/8 resemble those caused by compromised EGFR/MAPK and BMP signaling, respectively, we assessed the activities of these pathways in larval wing imaginal discs using antibodies specific for the activated forms of the MAPK (pMAPK)[72] or Mad (pMad) pathway effectors.[73] Paralleling the observed adult phenotypes, wing discs expressing NSP3 displayed greatly reduced pMAPK staining (Figure 4D), as observed previously with anthrax lethal factor.[74] Similarly, wing discs expressing NSP6 or NSP8 exhibited reduced levels of pMad staining (Figures 4E and S4). These congruent observations, linking reduced activities of specific signaling pathways in larvae with adult phenotypes, indicate that the viral factors are likely to disrupt these canonical signaling pathways.

NSP3 and NSP5 are proteases (PLpro and 3CLpro, respectively) that process the primary SARS-CoV-2 pp1a and pp1ab polyproteins. We wondered whether the catalytic activities of these enzymes are required for producing wing phenotypes. For NSP5, the p.C145A mutation of a critical catalytic residue greatly diminishes phenotype severity (Figure S5A), suggesting that NSP5 cleaves essential host proteins. In contrast, the p.C857A mutation of NSP3 did not alter its activity, revealing that NSP3 protease activity is not required to produce its wing phenotype (Figure S5B). These different outcomes highlight the utility of the DCR and sensitive wing assays to parse out contributions of specific domains or the relevance of catalytic activities of viral proteins.

NSPs exhibit potent synergistic interactions in the wing

Some SARS-CoV-2 proteins have been shown to physically bind to each other,[10,75–78] although the functional consequences of these interactions on host cells remain to be determined. An informative approach for identifying viral factors working in concert is to co-express them and test for potential synergistic or inhibitory interactions.

We expressed NSPs in pairwise combinations in the developing wing, focusing our analysis on NSPs producing viable offspring with the wingGAL4 driver (NSP2, NSP6, and NSP7–10). We observed several consistent cooperative interactions among these viral factors resulting in much more severe phenotypes than those produced by individual NSPs. While weak to moderate-strength genetic interactions were observed in some pairwise combinations (NSP2–NSP9, NSP2–NSP7, and NSP2–NSP10, Figure 5E), NSP8 stood out

by exhibiting strong interactions with several other NSPs, most notably synergizing with NSP6, NSP7, NSP9, and NSP10 (Figure 5). When expressed at submaximal levels (+++), NSP7, NSP9, and NSP10 generated no phenotypes on their own. However, when combined with NSP8, they each strongly enhanced its wing phenotype (Figures 5A and 5B). Similarly, under weaker expression conditions where NSP6 by itself caused a moderate phenotype (Figure 5C) and NSP8 alone caused no phenotype, co-expression of NSP6–NSP8 resulted in a strong enhancement (Figures 5C and 5D). Since NSP6 and NSP8 each produce BMP-like phenotypes (Figures 4C, 4E, and S4), their synergistic interaction presumably reflects converging effects on this pathway.

The interaction of NSP8 with NSP7 is also informative because NSP7 does not generate any phenotype even when expressed at the highest levels. Thus, its synergism with NSP8 reveals its activity in wing cells. This genetic interaction is consistent with prior studies indicating its direct binding to NSP8 to form a hexadecamer complex.[77,78] Thus, with its multiple synergies revealed in the wing, NSP8 appears to act as an interaction hub, coordinating some of the activities of NSP6, NSP7, NSP9, and NSP10 *in vivo*. We conclude that the *Drosophila* wing is a sensitive system for detecting specific functional connections among NSPs.

NSPs functionally interact with some human host factors identified by mass spectrometry

Comprehensive proteomic studies have identified a multitude of human proteins that may engage in virus-host interactions.[7–10,12] These proteome-wide studies call for further analysis to establish which of these many physical interactions have functional relevance *in vivo* and how they may contribute to viral infection. Because NSP8 emerged as a central hub interacting with four other NSPs (Figure 5), we examined potential functional connections between NSP8 and its human binding candidates.[8,9] Twenty-four host proteins were reported to bind to NSP8,[9] including constituents of the mitochondrial ribosome, exosome components, signal recognition particle (SRP) subunits, and other activities (Figure 6A). We expressed each of the 17 available individual human NSP8-interacting proteins alone or with NSP8 in the wing. Nine of these factors did not modify the baseline NSP8 wing phenotype, nor did they cause any phenotype alone (Figure S6A). In contrast, seven factors (ATE1, NSD2, EXOSC2, EXOSC5, NARS2, DDX10, and MRPS27) enhanced the NSP8 phenotype to varying degrees (Figures 6A–6C, S6B, and S6C), and only SRP19 produced a weak suppression of the NSP8 phenotype. When expressed alone, most of these genes had no effect except for NSD2 and EXOSC2, which produced mild and moderate small wing phenotypes, respectively. Consistent with EXOSC2 and NSP8 interacting strongly, the phenotypes of EXOSC2 were significantly exacerbated by co-expression with NSP8 even under conditions of lower expression where NSP8 had little effect alone (Figure S6C, right panel). Among the most notable enhancers of the NSP8 phenotype were EXOSC5 and EXOSC2, two components of the RNA exosome complex,[79] and ATE1, an arginyltransferase that modifies specific proteins to alter their activity or targets them for degradation.[80] Most dramatically, co-expression of ATE1 with NSP8 reduced wings to a mere rudiment (Figures 6B and 6C). Consistent with this synergism, RNAi knockdown of the endogenous *Drosophila* ortholog of *ATE1* (*Ate1*) with either of two independent lines resulted in robust suppression of the NSP8 phenotype, indicating that this protein is an important mediator of basal NSP8 activity in the wing (Figures 6B and 6C). We find that

the *T2A-GAL4* insertion into the *Ate1* locus is homozygous lethal, suggesting that *Ate1* is an essential *Drosophila* gene. Expression of *ATE1* driven by the *T2A-GAL4* in an *Ate1* mutant background partially rescued this lethality (Figure S7), demonstrating that fly *Ate1* and human *ATE1* are functionally conserved.

NSP8 synergizes with ATE1 to induce actin arginylation and cytoskeletal alterations

Our results indicate that NSP8-induced wing phenotypes are in part mediated by *Ate1*. Protein arginylation plays various roles including regulation of cytoskeletal dynamics, particularly the F-actin network, during embryogenesis, cardiovascular development, and angiogenesis.[81,82] Furthermore, the actin cytoskeleton is disrupted during infection with SARS-CoV-2, as illustrated by characteristic spherical inclusions in SARS-CoV-2-infected pulmonary cells.[83] We therefore evaluated the impact of NSP8 and ATE1 on the actin cytoskeleton. In wild-type wing imaginal discs, polymerized F-actin was primarily restricted to an apical band underlying intercellular junctions as revealed by phalloidin staining. Fainter F-actin lines along the plasma membrane extending along the apico-basal axis were also observed (Figure 7A, left panel). This pattern was mildly altered in wing discs expressing either NSP8 or ATE1. NSP8 induced formation of a few intracellular F-actin foci (Figure 7A, second panel), whereas ATE1 produced irregular vertical F-actin labeling. These mild cytoskeletal phenotypes were notably enhanced by co-expression of ATE1 and NSP8, which profoundly disrupted the apical F-actin network and caused the appearance of many scattered F-actin-rich inclusions (Figure 7A, rightmost panel).

We also examined salivary glands, for which high levels of F-actin mark the cell borders in control tissues. When expressed, NSP8 or ATE1 resulted in the appearance of ectopic cytoplasmic F-actin-rich inclusions (Figure 7B). Co-expression of NSP8 and ATE1 exacerbated these defects, resulting in a more irregular cortical F-actin network and in numerous atypical F-actin rings, similar to those reported in SARS-CoV-2-infected human cells,[83] as well as long F-actin filaments traversing the cytoplasm. We conclude that NSP8 acts in concert with ATE1 to disrupt F-actin organization in both wing discs and salivary glands.

We next examined whether NSP8/ATE1 induced arginylation of actin using an antibody specific for arginylated β-actin (R-actin)[84] for western blot and immunofluorescence analysis. In extracts from control adult flies (hs-GAL4/+), only a faint R-actin signal could be detected (42 kDa). Heat-shock-induced expression of NSP8 or ATE1 alone led to moderate increases in R-actin, while co-expression of NSP8 with ATE1 substantially elevated R-actin levels (Figure 7C, left panel), mirroring their strong positive phenotypic interactions observed in adult and larval wings. Actin arginylation increased sequentially following a single heat shock, indicating that this process is progressive (Figure 7C, right panel).

We also examined *in situ* actin arginylation in response to NSP8 and ATE1 co-expression in salivary glands. In control glands, we observed a unique subcellular distribution of R-actin relative to the F-actin network. R-actin in these cells displayed a punctate cytoplasmic staining pattern but also accumulated at intercellular junctions, particularly where the cortical F-actin stain was weaker, indicating that R-actin and F-actin have distinct but

adjacent localization patterns (Figure 7D, left panels, arrows). In glands co-expressing NSP8 and ATE1, R-actin and F-actin co-localized in irregular cortical accumulations (Figure 7D, right panels, arrows). In addition, R-actin labeled a subset of ectopic F-actin cytoplasmic rings/spheres induced by NSP8/ATE1 co-expression (arrowheads), typically among those showing fainter F-actin labeling. Overall, the above experiments indicate that NSP8 activity is mediated to a great extent by ATE1. We tested this hypothesis further by feeding developing flies expressing NSP8 with suramin or merbromin, two chemical inhibitors of the ATE1 enzyme.[85] Both compounds, which have been also shown to reduce SARS-CoV-2 viral loads in cell-based infections,[86,87] ameliorated the NSP8 wing phenotype and did so in a cooperative fashion (Figure 7E). Cumulatively, these phenotypic, biochemical, and immunofluorescence data support a model in which ATE1 acts as a critical mediator of NSP8 activity, inducing actin arginylation, disrupting F-actin organization and producing ectopic F-actin-rich ring-like structures.

DISCUSSION

Human cells, organoids, and mammalian model organisms including mice, hamsters, minks, ferrets, shrews, and non-human primates have been used to study COVID-19.[88] While systemic infection of a mammalian model organism with SARS-CoV-2 can cause phenotypes reminiscent of disease symptoms in humans, it is often difficult to elucidate the precise molecular mechanisms underlying specific pathologies. In this study, we addressed these challenges by generating the DCR resource in *Drosophila* that enables multi-faceted parallel *in vivo* studies of virus-host interactions for SARS-CoV-2 to greatly accelerate the pace of research in this field.

Expression of individual viral genes can induce phenotypes that are sometimes very similar to those resulting from altered function of a fly gene,[13,14] pointing to potential biological processes or signaling pathways affected by the viral protein. In addition, if the human cDNA can rescue the loss of the fly gene, a compelling case can be made to study the function of the viral genes and their targets *in vivo* using *Drosophila* to guide further mechanistic analyses in vertebrates. The above reagents may also provide a robust platform to screen for drugs that suppress the phenotypes induced by UASSARS-CoV-2 genes or suppress the phenotypes associated with L-o-F mutations of the viral target gene. Similar approaches to suppress phenotypes associated with rare genetic disease have identified several Food and Drug Administration-approved drugs in flies.[89–92] Expression of seven SARS-CoV-2 encoded proteins using three different ubiquitous drivers caused lethality. Our study identifies the most toxic factors as NSP1, NSP3, NSP5, NSP13, NSP15, Orf3a, and Orf6, which induce lethality with three ubiquitous GAL4. These findings mirror to a large extent results from a fission yeast study in which these factors caused cell death and inhibited proliferation, suggesting that they act on broadly conserved targets.[58] Although it remains to be determined whether lethality in flies is caused by mechanisms that relate to mortality caused by COVID-19, lethality is a simple and robust phenotype to assess. We envision that screens to revert such lethality could be used to identify genes or small molecules that suppress the toxic effect of a viral protein.

Photoreceptor-specific overexpression experiments revealed that six out of seven SARS-CoV-2 proteins that cause lethality when ubiquitously expressed disrupt neuronal function in the visual system. Studies in monkeys have shown that SARS-CoV-2 affects cortical regions of the brain that receive direct olfactory input, suggesting that the virus may enter via the nose to infect neurons.[93] Such SARS-CoV-2 brain infections lead to neuroinflammation and neurodegeneration, a mechanism that may contribute to PASC in humans. PASC includes symptoms that relate to neuronal dysfunction including fatigue, headaches, memory impairment, and decreased concentration.[94,95] Since fly photoreceptors are amenable to many experimental assessments including histological and ultrastructural analysis,[96] this approach may provide molecular insights into how neurons are impacted in COVID-19 and PASC. Interestingly, six viral proteins cause age-dependent ERG defects, indicating that continuous long-term expression of these viral proteins causes progressive neuronal dysfunction.

Early-expressed NSPs generate distinct instructive wing phenotypes

Distinctive wing phenotypes induced by viral factors complement functional information obtained from lethality assays. Patterning defects can be diagnostic for disruption of known signaling pathways, providing clues for further functional analysis. For example, NSP3 adult phenotypes suggest impairment in EGFR/MAPK signaling, and NSP3 reduces downstream MAPK activation in wing vein primordia. Similarly, NSP6 and NSP8 generated vein-fusion phenotypes similar to those caused by reduced activity of the BMP (Dpp in flies) pathway[64,65] or expression of BMP antagonists.[65,97] Strengthening our observations, these two NSPs also reduced levels of pMAD, the primary BMP signaling transducer. Interestingly, SARS-CoV-2 infections trigger expression of transforming growth factor β (TGF-β) and BMP antagonists,[98–100] associated with damaging inflammation, apoptosis, and fibrosis.[101] Thus, modulation of TGF-β/BMP signaling components by NSP6 and NSP8 during infection could be evaluated as targets for therapeutic intervention.[102] Expression of other NSPs caused thickened veins typical of reduced Notch signaling (NSP4), blistering reflective of impaired cell adhesion (NSP1, NSP5), or ectopic veins (NSP9, NSP10), which could reflect ectopic MAPK or BMP pathway activation. Future molecular and genetic epistasis experiments should help define specific host components mediating the effects of individual NSPs to explore the connection between these activities and COVID-19.

Phenotypic analysis distinguishes activities of variant SARS-CoV-2 proteins

A defining feature of viruses is their ability to rapidly evolve, a characteristic which has proved to be a particular challenge in the case of SARS-CoV-2. Expression of SARS-CoV-2 proteins in *Drosophila* offers an avenue for assessing the functional effect of naturally occurring variants as well as for testing the role of specific amino acid residues using synthetically produced mutations. In this study, we provide two examples demonstrating the potential to resolve differing activities of SARS-CoV-2 protein variants in *Drosophila*.

First, we examined the phenotypic consequence of an ORF3a mutation (p.Q57H) that has been detected in multiple SARS-CoV-2 strains.[103] Our data indicate that the p.Q57H allele is less toxic to host cells than the reference allele in several settings. A possible interpretation for this result is that the weaker p.Q57H allele may have been selected

because it promotes net viral infectivity. As has been demonstrated with other COVID strains, viral transmissibility and lethality can be tradeoffs: less-virulent strains frequently spread faster than those that are more lethal.[104] It should be informative to extend such functional analyses to variants arising in other SARS-CoV-2 encoded proteins reported in the CoV-GLUE-Viz database (http://vshiny1.cvr.gla.ac.uk/cov-glue-viz/). Similarly, we compared catalytically active and inactive forms of NSP3 and NSP5 proteases using the wing phenotype assay. We found that the NSP3 phenotype was independent of its protease activity. Further epistasis experiments using information from a recent NSP3 interactome study[105] should help define which host proteins may be functionally relevant for this phenotype. Of note, stress sensor ATF6, a protein that binds to NSP3[106] and regulates MAPK signaling,[107] is a prime candidate for further analysis. In contrast, the catalytically inactive NSP5$^{p.C145A}$ caused a much milder wing phenotype compared to the reference NSP5. It will be informative to determine which host proteins are cleaved by NSP5 to mediate its phenotype. Candidates identified in a recent bioinformatics study should be considered for future functional screens.[106]

NSPs interact synergistically with each other

NSPs form various complexes with each other to exert specific effector functions.[10,75–78,108–110] In our initial survey of genetic interactions among NSPs in the wing, NSP8 stood out as a central “hub,” strongly interacting with several other NSPs. We note that both NSP7 and NSP9 are known to engage in direct protein-protein interactions with NSP8. Regarding NSP10, it has been reported to interact with the host protein CAND1, which also binds to NSP8[10] and could potentially mediate the NSP8/NSP10 synergism. Alternatively, NSPs may impact distinct but intersecting pathways, potentially resulting in some of the observed genetic interactions.

NSP8 interacts *in vivo* with a subset of human candidate proteins

The prime motivation for developing the DCR was to determine which human interactors identified by proteomic studies are functionally relevant. We note that among interactors identified in the first interactome study,[9] 44% are found at least once again in independent comparable studies (Table S5; Chen et al.,[7,10–12] Li et al.,[7,10–12] Stukalov et al.,[7,10–12] Zhou et al.[7,10–12]). The broad diversity of binding partners identified in multiple independent studies calls for additional functional tests, including functional interrogation screens, or co-expression experiments such as those described here. In the case of NSP8, 24 human NSP8-interacting proteins were identified in an initial systematic study.[9] Taking advantage of the DCR toolbox, we observed seven positive interactions and one suppression out of the 17 UAS-h-cDNA lines available. Two of the strongest interactors (EXOSC2 and EXOSC5) belong to the RNA exosome, which mediates degradation of various types of RNA molecules.[111,112] Interestingly, low expression of EXOSC2 has also been recently identified through genome-wide association studies to be protective against SARS-CoV-2 infection.[113] Other noteworthy NSP8 interactors include DDX10, a member of the of DEAD box family of RNA helicases, which contain regulators of SARS-CoV-2 infection,[114,115] and NSD2, a histone methyltransferase which dimethylates nucleosomal histone H3 to regulate chromatin integrity and gene expression.[116] We note that among the seven interactors

identified in our experiments, only MRPS27 has been validated in a functional interrogation screen.

NSP8 synergizes with ATE1 to arginylate actin and disrupt F-actin networks

The strongest NSP8 interactor we identified was ATE1, an arginyltransferase which, when co-expressed with NSP8, produced a strong synergistic rudimentary wing phenotype. Conversely, the NSP8 phenotype was potently suppressed by knockdown of fly *Ate1* or by two known inhibitors of human ATE1,[85] suggesting that a key cellular activity of NSP8 depends on this host arginyltransferase. ATE1 is known to act on several cytoskeletal proteins, including actin, to regulate F-actin levels and dynamics.[82] Here we observed abnormal ring-shaped F-actin structures formed in response to NSP8/ATE1 co-expression, reminiscent of those induced by SARS-CoV-2 infection in pulmonary cells,[83] presumably resulting from misregulated arginylation. These spherical structures may correspond to vesicles derived from the cell surface or from internal organelles. We note that the underexplored arginylation pathway plays roles in several processes relevant to SARS-CoV-2-induced pathogenesis, such as coagulation,[117] cardiac inflammation and fibrosis,[118] cellular respiration,[119] ER stress,[120,121] and neural activity.[119,122] Consistent with ATE1 playing a role during infection, a recent study finds that the ATE1 protein levels are increased in cultured cells infected by SARS-CoV-2 and that ATE1 inhibitors (suramin, merbromin, and tannic acid), as well as *ATE1* silencing, reduce viral loads.[86,87] Moreover, SARS-CoV-2 patients show alterations in their global arginylation landscape.[123] Altogether, these elements support the idea that the ATE1/NSP8 tandem plays a relevant role during SARS-CoV-2 infection and represents an attractive therapeutic target.

In conclusion, we provide the research community with the comprehensive DCR resource to enable functional analysis of all SARS-CoV-2 factors in *Drosophila*. The examples delineated above illustrate possible routes to explore the activities of these factors, although additional organs/tissues could be employed. A key aspect of these investigations lies in identifying which human proteins mediate viral activities and establishing the function of these host partners. The reagents described here should facilitate unraveling of the multiple impacts of SARS-CoV-2 factors on host proteins.

Limitations of the study

In this report we express viral factors in various *Drosophila* tissues, either alone or in combination with dedicated human partners, identified in a proteomics screen.[9] Although a live organism offers many benefits as compared to cultured cells, we are aware that results obtained from an insect model require validation in other contexts, such as human cells or mammalian model organisms. Also, the synergistic phenotypes we show in this study may not necessarily reflect direct physical interactions: the interacting factor could be part of larger protein complexes or impinge on a common pathway. We also note that our study focused on a limited set of SARS-CoV-2 interacting proteins identified by Gordon et al.[9] Other screens[7,10–12] have identified 1,693 additional interactors. Because of our past efforts to generate human cDNA transgenic resources, 551 additional lines are available, covering nearly one-third of all proteins identified in these screens (Table S5).

STAR★METHODS

RESOURCE AVAILABILITY

Lead contact—Further information and requests for resources and reagents should be directed to and will be fulfilled by lead contact Hugo Bellen (hbellen@bcm.edu).

Materials availability—The list of the UAS-SARS-CoV-2 transgenic flies generated in this study can be found in Table S1. The available UAS-human cDNA stocks encoding SARS-CoV-2 protein interactors generated in this study are listed in Table S2. The available T2A-GAL4 or Kozak-GAL4 lines for fly ortholog candidates that encode for SARS-CoV-2 human interactors are listed in Table S3. All newly generated reagents have been deposited at BDSC or KDSC. Stock numbers are indicated in Tables S1–S3.

Data and code availability—The sequencing information and PCR verification of T2A-GAL4 and Kozak-GAL4 lines are available from the *Drosophila* GDP (Gene Disruption Project) Website (https://flypush.research.bcm.edu/pscreen/index.php). This paper does not report original code. Any additional information required to reanalyze the data reported in this paper is available from the lead contact upon request. Tables S1–S5 are available at Mendeley Data: https://data.mendeley.com/datasets/4p3m97pkkx/1.

EXPERIMENTAL MODEL AND SUBJECT DETAILS

Fly stocks—All *Drosophila melanogaster* flies used in this study were generated in house or obtained from the Bloomington Drosophila Stock Center (BDSC), Vienna Drosophila Resource Center (VDRC) or Kyoto Drosophila Stock Center (KDRC) and reared on standard fly food. The names of each fly line that are not listed in Tables S1–S3 are listed below along with their genotypes and source information.

Fly line	Genotype	Source
Act-GAL4	*y^1 w*; P{Act5C-GAL4}17bFO1/TM6B, Tb^1*	BDSC #3954
Tub-GAL4	*y^1 w*; P{w[+mC]=tubP-GAL4} LL7/TM3, $Sb^1 Ser^1$*	BDSC #5138
da-GAL4	*w*; P{w[+mW.hs]=GAL4-da.G32}UH1, Sb^1/TM6B, Tb^1*	BDSC #55851
MS1096-GAL4	*w^{1118}P{w[+mW.hs]=GAL4}Bx[MS1096]*	BDSC #8860
Hs-GAL4	*w*; P{w[+mC]=GAL4-Hsp70.PB}89-2-1*	BDSC #1799
UAS-Empty	*y^1 w*; PBac{UAS-empty}VK37/SM6a*	Goodman et al., 2021
Rh1-GAL4	*P{ry[+t7.2]=rh1-GAL4}3, ry[506]*	BDSC #8691
Ate1 $^{CRIMIC\text{-}TG\ 4}$	*y^1* w*; *TI{CRIMIC.TG4.0}Ate1CR00893-TG4.0/SM6a*	BDSC #81152
Ate1-Df	*w^{1118}; Df(2R)Exel7162/CyO*	BDSC #7896
Ate1-RNAi	y1 *sc** v1 sev21; *P{TRiP.GLC01821}attP2*	BDSC #53867
Ate-RNAi	*P{KK107889}VIE-260B*	VDRC #104360

METHOD DETAILS

SARS-CoV-2 UAS-cDNA generation, related to Figure 2B—The UAS-cDNA lines expressing SARS-CoV-2 viral protein were generated using standard methodologies.[44]

Briefly, the open and close versions of Gateway-compatible entry vectors, which were deposited by Fritz Roth Lab,[28] were obtained from Addgene. The cDNAs were transferred to the pGW-HA.attB destination vector using LR clonase II (ThermoFisher #11791020). All clones were confirmed with Sanger sequencings. Since *NSP11* is too short to be compatible with the Gateway cloning system, the *NSP11* cDNA (with or without a stop codon) was inserted into the pGW-HA.attB empty plasmid by Q5 site-directed mutagenesis (New England Biolabs) with primers listed below. The whole plasmid sequencing based on the Sanger method confirmed to be no second site mutations. These constructs were inserted into the VK37 docking site using φC31-mediated transgenesis[33] and balanced using *SM6a*. Final genotype:

y^{1} *w**; *PBac{y*[+*mDint2*] *w*[+*mC*]=*UAS-SARS-CoV-2* cDNA*}VK00037*/(*SM6a*), or

y^{1} *w**; *PBac{y*[+*mDint2*] *w*[+*mC*]=*UAS-SARS-CoV-2* cDNA-*HA}VK00037*/(*SM6a*).

NSP11 constructs	Primers for mutagenesis
UAS-NSP11	Forward: ttttaaacgggtttgcggtgtaaAACCCAGCTTTCTTGTACAA
	Reverse: acgattgtgcatcagctgaCATGGTGCCTGCTTTTTTGTACA
UAS-NSP11-HA	Forward: ttttaaacgggtttgcggtgAACCCAGCTTTCTTGTACAA
	Reverse: acgattgtgcatcagctgaCATGGTGCCTGCTTTTTTGTACA

UAS-Kozak-NSP1-10 constructs were generated from the Addgene plasmid collection (#141255–141264). For each cDNA, a PCR fragment was generated with primers adding the CACC Kozak sequence right before the ATG start codon, and complementary overhangs for insertion into thepUASTattB vector (Addgene) downstream of the UAS(5X)/hs promoter sequences. The NEBuilder HiFi DNA Assembly kit (#E5520) was used to assemble PCR fragments, and the final sequence was verified.

MUTAGENESIS OF ORF3a, NSP3 AND NSP5

For ORF3a^{Q57H} mutagenesis, the ORF3a reference plasmid was obtained from Addgene (Addgene #149319). The variant was introduced using the Q5 site directed mutagenesis kit according to the manufacturer's protocol (NEB# E0554). Briefly, gateway compatible constructs were transformed using high efficiency E. coli competent cells (NEB# C2987H) and successful mutagenesis was confirmed by Sanger sequencing the region of interest. The pDONR 207 entry vector was then transferred to the pGW-attB-3xHA.attB destination vector using LR clonase II (ThermoFisher #11791020), constructs were again transformed into high efficiency E. Coli competent cells, and the full sequences were confirmed by Sanger sequencing prior to injection. These constructs were inserted into the VK37 docking site using φC31-mediated transgenesis[33] and balanced using *SM6a*.

ORF3a constructs	Primers for mutagenesis
UAS-ORF3a p.Q57H-HA	Forward: CCGTGTTCCAtTCCGCCTCTAAGATCATC

ORF3a constructs	Primers for mutagenesis
	Reverse: CCAGCAGGGCCACACCCA

For mutant NSP3 (C857A), the UAS-Kozak-NSP3 plasmid was digested with Sbf1 and Stu1. The 1.6Kb fallout fragment was replaced with homologous DNA containing the 3nts C857A mutation and two complementary overhangs flanking the Sbf1 and Stu1 sites (30 nts on each side, gBlocks synthesized by IDT). Replacement was realized with NEBuilder kit, and sequence was verified. Similarly, for mutant NSP5 (C145A), the UAS-Kozak-NSP5 plasmid was digested with EcoRI and EcoNI, and the 0.6Kb fallout was replaced with a 0.6Kb DNA containing the C145A mutation and complementary overhangs.The constructs were inserted on the third chromosome docking site (attP2-3L68A4). Positive transformants were identified through the mini-*white* marker in the eyes and the inserted cassette was sequenced after PCR amplification of genomic sequences.

UAS-human cDNA generation—Gateway compatible full length human cDNA clones in pDONR221 or pDONR223 were obtained from a public Mammalian Gene Collection[124] or a commercial source (UltimateORF Clones, Thermo Fisher). The cDNAs were transferred to the pGW-HA.attB or pUASg-HA.attB destination vector using LR clonase II (ThermoFisher #11791020). All clones were validated by end sequencing. These constructs were inserted into the VK37, VK33[33] or ZH-86Fb[125] docking sites using φC31-mediated transgenesis[33] and balanced using *SM6a* or *TM3 Sb Ser*. In principle, we injected the transgenes on to VK37 (second chromosome docking site) if the best fly ortholog candidate of the human gene was located on the X, third or fourth chromosome. If the best fly ortholog candidate was located on the second chromosome, we injected them into VK33 or ZH-86Fb (third chromosome docking sites, latter being used during the early phase of the project). Two transgenes were inserted on *attP40*[126] or *VK02*[33] (both second chromosome docking sites), respectively, since they were generated during the pilot phase of this project. Second chromosome transgenes were balanced using *CyO* or *SM6a*, and third chromosome transgenes were balanced using *TM3*, *Sb*, *Ser* or *TM6b*, *Hu*, *Tb*, respectively.

T2A-/Kozak-GAL4 generation—T2A-GAL4 and Kozak-GAL4 CRISPR mediated homologous recombination alleles are generated using partially synthesized homology donor intermediates.[26,32] Briefly, 200 bps of homology arms are synthesized in pUC57_Kan_gw_OK vector by Genewiz/Azenta to generate homology donor intermediates. T2A-GAL4 or Kozak-GAL4 cassette is subcloned from pM37/pM37_kG4 vector respectively to the homology donor intermediate vector in BbsI or BsaI site Int200-T2AGAL4 and int200-KozakGAL4 constructs were injected at 250 ng/μL along with 100 ng/μL gene-specific gRNA(s) cloned in pCFD3 or pCFD5, respectively together with sgRNA1 (targeting GTAGTACGATCATAACAACGCGG) to linearize the homology donor construct.[127,128] To generate homology donor intermediates of int200_gRNA_T2A-GAL4 or int200_gRNA_Kozak-GAL4 lines, 200 bps homology arms and gene specific sgRNAs are commercially synthesized by Genewiz/Azenta. T2A-GAL4 or Kozak–GAL4 cassette is subcloned from pM37/pM37_kG4 vector respectively to the homology donor intermediate vector in BbsI or BsaI site int200-gRNA_T2AGAL4 and int200_gRNA_KozakGAL4

constructs are injected at 250 ng/ul final concentration. Injections of 400–600 embryos from y1w*; iso18; attP2(y+){nos-Cas9(v+)} for genes on the second or fourth chromosome and y1w* iso6 attP2(y+){nos-Cas9(v+)} for genes on the X chromosome and y1w*; attP40(y+){nos-Cas9(v+)}; iso5^{129} for genes on the third chromosome were injected. Whole genome sequencing BAM files of isogenized lines can be found at https://zenodo.org/record/1341241. Resulting G0 males and females were crossed individually to y^{1} w^{*} flies as single fly crosses for 3XP3-EGFP detection. Positive lines were balanced, and stocks were established. Up to five independent lines were generated per construct per gene. The list of generated alleles can be found in Table S3. The sequences of homology arms and sgRNA(s) as well as the results of PCR validation and imaging on third instar larval brain are available at https://flypush.research.bcm.edu/pscreen/crimic/crimic.php. The stocks are deposited in the Bloomington Drosophila Stock Center (BDSC) on a regular basis. The stocks are available from the Bellen lab until they are deposited and established in the BDSC. Lines generated through RMCE of MiMIC alleles are generated through genetic crossing strategy.[27,37,130]

Lethality assessment, related to Figures 3, S2, and S3—Crosses for assessment of lethality and morphological phenotypes were performed using the GAL4 drivers indicated in the text. Crosses were established using 5–10 virgin females crossed to a similar number of males. Parents were transferred to a new vial every 3–7 for multiple collections of progenies. Flies were collected after eclosion and genotypes were assessed based on the absence of balancers. When majority of the relevant progenies eclose and do not have obvious defect in movement and morphology, the combination is defined as viable. When some die before eclosion while there are also surviving adults, the lines are defined as semi-lethal. When there are no eclosions, the lines are defined as lethal. For lethal crosses, staging of lethality was performed based upon the oldest stage reached by the majority of flies. If no larvae were observed, the cross was recorded as embryonic lethal.

Wing phenotype assessment, related to Figures 3, 4, and 5—Wings were stored in isopropanol until mounting in Canada balsam (Sigma Aldrich Cat#101691). Pictures were taken with a 34x zoom factor using a Zeiss AXIO Zoom.V16 microscope, and further adjusted on Photoshop (21.2.4). Surface area was measured in FIJI (ImageJ 1.53t) using the “Ellipse Selection” followed by the command “Measure”. Data was exported to GraphPad Prism (version 9.4.1), for statistical analysis and graphs. Comparison between two conditions were tested with the Unpaired t test and between three or more conditions with Ordinary one-way ANOVA.

ERG assessment, related to Figure S1—ERG recordings were performed using standard procedures.[45] Briefly, after eclosion, flies were maintained at 25°C with 12-h light (~3,500 Lux)/dark cycle before the recording. The flies were immobilized on a glass slide with glue. A recording electrode filled with 150 mM NaCl was placed on the surface of the eye while a reference electrode was placed in the thorax. Repeated light/ dark stimulations were given during the recording, and the response of photoreceptors were digitized using LabChart 8 software. We use the UAS-Empty as a control line, generated by injecting the pGW-HA.attB plasmid without an insertion into VK37.[131]

Western blotting, related to Figures 7, S2, and S3—For WB in Figure 7C, adult flies (1–2 days-old) were heat shocked at 37°C for 90 or 120 min. After a rest at RT of varying durations, groups of 10 flies were homogenized in 100 μL RIPA buffer with protease inhibitors. Cuticles and insoluble matters were eliminated by centrifugation at 4°C. For WB in Figure S3, L3 larvae were homogenized into RIPA Lysis and Extraction Buffer (Thermo Scientific) at 25 μL per larva. Proper amount of 4x Laemmli Sample Buffer (Bio-Rad) was added. 10 μl of lysate samples were loaded on SDS-PAGE, 4%–12% Mini-PROTEAN TGX Precast Gel (Bio-Rad) gels. After separation, proteins were transferred onto PVDF membranes (Millipore). Membranes were incubated with the corresponding primary and secondary antibodies and signal was obtained using Supersignal chemiluminescent substrate (Thermo Fisher # 34580). All antibodies used are documented in the key resources table. For protein quantifications in Figures S2 and S3, protein levels were analyzed by ImageJ.[132] Briefly, the optical densities of bands were quantified and the density ratio of each immunoreactive band to the corresponding Actin band was calculated. The results were presented as relative fold changes.

Immunostaining, related to Figures 4, 7, S4, and S7—For immunostainings, wing imaginal discs and salivary glands were dissected from L3 wandering larvae, fixed for 20 min in 4% formaldehyde in PBS, washed and blocked in 1% BSA PBS. Primary antibody was added at 1:100 dilution overnight at 4°C. Secondary incubations was at 1:400 for 2 h at RT and nuclear DAPI staining (Thermo Fisher #D1306) for 30 min at RT. The antibodies used were anti-pMad (Cell signaling, #9516), anti-pMAPK (Cell signaling, #4377), anti R-actin (Millipore #ABT264). For F-actin stain, 647-Phalloidin (Thermo Fisher #A22287, 1:200) was added with secondary antibodies (Thermo Fisher Alexa 488 anti Rabbit IgG, #A 21–200). Stained tissues were mounted in Slowfade Gold Antifade Mountant (Life Technologies #S36936), with a double-sided tape between slide and the coverslips for salivary glands to avoid crushing. Imaging was performed on a Leica TCS SP8 confocal microscope. For brain and wing disc imaging the larvae were dissected in PBS and fixed 20 minues in 4% formaldehyde in PBS. Samples are washed and blocked with PBS 0.3% Triton X-100 5% Normal Donkey Serum (NDS). Primary antibody (anti-mCherry, Genetex #GTX59788) was incubated at 1:200 dilution in PBS 0.3% Triton X-100 5% NDS. Multistack images were taken and exported for processing on FIJI (ImageJ 1.53t). Final panels were created using Adobe Photoshop software.

Drug treatments, related to Figure 7—Suramin and Merbromin were resuspended in H_2O to stocks of 5mM and 100mM, respectively. They were then diluted in 100% grape juice (Welch) to the appropriate concentrations. For each condition, 2mL of grape juice+drug was dispensed onto 1 gm of ground potato flakes placed in vials on top of regular brown fly food.

QUANTIFICATION AND STATISTICAL ANALYSIS

Statistical analysis was performed using GraphPad software (GraphPad Prism v9.0; GraphPad Software, USA). Statistical analysis was performed using Student’s t-test. Data are presented using scattered plots with each dot representing measurement of an independent biological sample. Number n of biological replicates is indicated on each

graph. Bars indicate mean with standard deviation. p values are indicated using standard symbolism: ns for $p > 0.05$; * for $p < 0.05$; ** for $p < 0.01$; *** for $p < 0.001$; and **** for $p < 0.0001$.

Supplementary Material

Refer to Web version on PubMed Central for supplementary material.

ACKNOWLEDGMENTS

We thank the Bloomington Drosophila Stock Center for providing numerous stocks and distributing the DCR to the community. We thank Sitara Roy, Gabriela Martins, and Saluja Kaduwal for technical help and advice. We thank Charles Yu, Michael Neff, Yoko Takashima, Ryan Kenneally, Joanne Eichenberger, and Quentin Lawrence for generating human expression clones. We thank the 4th Chromosome Resource Project (supported by R24OD028242) for sharing the *Actbeta*$^{MI14795\text{-}DH.GT\text{-}TG4.1}$ stock. This work was supported by NIH grants R24OD022005-07S1 (to H.J.B., M.F.W., and S.Y.), R24OD022005 (to H.J.B., S.E.C., and S.Y.), R24OD031447 (to H.J.B. and O.K.), R24OD031447-02S1 (to H.J.B. and O.K.), R01GM117321 (to E.B.), R01GM144608 (to E.B.), and R01AI162911 (to E.B.). We acknowledge financial support from the Kyoto Institute of Technology (T.T.-S.), as well as a gift from the Tata Trusts in India to TIGS-UCSD (to E.B.). S.Y., M.F.W., O.K., and H.J.B. are also supported by Jan and Dan Duncan Neurological Research Institute at Texas Children's Hospital. D.B. was supported by a CAPES fellowship (88887.659907/2021-00). Confocal microscopy at Baylor College of Medicine was supported by the Intellectual and Developmental Disabilities Research Center (grant no. U54HD083092) from the Eunice Kennedy Shriver National Institute of Child Health & Human Development. Confocal microscopy at UCSD was performed at the UCSD School of Medicine Microscopy Core (NINDS grant P30NS047101). The content is solely the responsibility of the authors and does not necessarily represent the official view of the funding agencies.

INCLUSION AND DIVERSITY

We support inclusive, diverse, and equitable conduct of research.

REFERENCES

1. Valencia DN (2020). Brief Review on COVID-19: The 2020 Pandemic Caused by SARS-CoV-2. Cureus 12, e7386. 10.7759/cureus.7386. [PubMed: 32337113]
2. Chen Y, Liu Q, and Guo D (2020). Emerging coronaviruses: Genome structure, replication, and pathogenesis. J. Med. Virol 92, 418–423. 10.1002/jmv.25681. [PubMed: 31967327]
3. Bavel JJV, Baicker K, Boggio PS, Capraro V, Cichocka A, Cikara M, Crockett MJ, Crum AJ, Douglas KM, Druckman JN, et al. (2020). Using social and behavioural science to support COVID-19 pandemic response. Nat. Human Behav 4, 460–471. 10.1038/s41562-020-0884-z. [PubMed: 32355299]
4. Korber B, Fischer WM, Gnanakaran S, Yoon H, Theiler J, Abfalterer W, Hengartner N, Giorgi EE, Bhattacharya T, Foley B, et al. (2020). Tracking changes in SARS-CoV-2 Spike: evidence that D614G increases infectivity of the COVID-19 virus. Cell 182, 812–827.e19. 10.1016/j.cell.2020.06.043. [PubMed: 32697968]
5. Dong S, Sun J, Mao Z, Wang L, Lu YL, and Li J (2020). A guideline for homology modeling of the proteins from newly discovered betacoronavirus, 2019 novel coronavirus (2019-nCoV). J. Med. Virol 92, 1542–1548. 10.1002/jmv.25768. [PubMed: 32181901]
6. Wang C, Liu Z, Chen Z, Huang X, Xu M, He T, and Zhang Z (2020). The establishment of reference sequence for SARS-CoV-2 and variation analysis. J. Med. Virol 92, 667–674. 10.1002/jmv.25762. [PubMed: 32167180]
7. Chen Z, Wang C, Feng X, Nie L, Tang M, Zhang H, Xiong Y, Swisher SK, Srivastava M, and Chen J (2021). Interactomes of SARS-CoV-2 and human coronaviruses reveal host factors potentially affecting pathogenesis. EMBO J 40, e107776. 10.15252/embj.2021107776. [PubMed: 34232536]

8. Gordon DE, Hiatt J, Bouhaddou M, Rezelj VV, Ulferts S, Braberg H, Jureka AS, Obernier K, Guo JZ, Batra J, et al. (2020). Comparative host-coronavirus protein interaction networks reveal pan-viral disease mechanisms. Science 370, eabe9403. 10.1126/science.abe9403.
9. Gordon DE, Jang GM, Bouhaddou M, Xu J, Obernier K, White KM, O'Meara MJ, Rezelj VV, Guo JZ, Swaney DL, et al. (2020). A SARS-CoV-2 protein interaction map reveals targets for drug repurposing. Nature 583, 459–468. 10.1038/s41586-020-2286-9. [PubMed: 32353859]
10. Li J, Guo M, Tian X, Wang X, Yang X, Wu P, Liu C, Xiao Z, Qu Y, Yin Y, et al. (2021). Virus-Host Interactome and Proteomic Survey Reveal Potential Virulence Factors Influencing SARS-CoV-2 Pathogenesis. Méd 2, 99–112.e7. 10.1016/j.medj.2020.07.002. [PubMed: 32838362]
11. Stukalov A, Girault V, Grass V, Karayel O, Bergant V, Urban C, Haas DA, Huang Y, Oubraham L, Wang A, et al. (2021). Multilevel proteomics reveals host perturbations by SARS-CoV-2 and SARS-CoV. Nature 594, 246–252. 10.1038/s41586-021-03493-4. [PubMed: 33845483]
12. Zhou Y, Liu Y, Gupta S, Paramo MI, Hou Y, Mao C, Luo Y, Judd J, Wierbowski S, Bertolotti M, et al. (2023). A comprehensive SARS-CoV-2-human protein-protein interactome reveals COVID-19 pathobiology and potential host therapeutic targets. Nat. Biotechnol 41, 128–139. 10.1038/s41587-022-01474-0. [PubMed: 36217030]
13. Smelkinson MG, Guichard A, Teijaro JR, Malur M, Loureiro ME, Jain P, Ganesan S, Zúñiga EI, Krug RM, Oldstone MB, and Bier E (2017). Influenza NS1 directly modulates Hedgehog signaling during infection. PLoS Pathog 13, e1006588. 10.1371/journal.ppat.1006588. [PubMed: 28837667]
14. Link N, Chung H, Jolly A, Withers M, Tepe B, Arenkiel BR, Shah PS, Krogan NJ, Aydin H, Geckinli BB, et al. (2019). Mutations in ANKLE2, a ZIKA Virus Target, Disrupt an Asymmetric Cell Division Pathway in Drosophila Neuroblasts to Cause Microcephaly. Dev. Cell 51, 713–729.e6. 10.1016/j.devcel.2019.10.009. [PubMed: 31735666]
15. Shah PS, Link N, Jang GM, Sharp PP, Zhu T, Swaney DL, Johnson JR, Von Dollen J, Ramage HR, Satkamp L, et al. (2018). Comparative Flavivirus-Host Protein Interaction Mapping Reveals Mechanisms of Dengue and Zika Virus Pathogenesis. Cell 175, 1931–1945.e18. 10.1016/j.cell.2018.11.028. [PubMed: 30550790]
16. Yamamoto S, Jaiswal M, Charng WL, Gambin T, Karaca E, Mirzaa G, Wiszniewski W, Sandoval H, Haelterman NA, Xiong B, et al. (2014). A drosophila genetic resource of mutants to study mechanisms underlying human genetic diseases. Cell 159, 200–214. 10.1016/j.cell.2014.09.002. [PubMed: 25259927]
17. Bier E, and Guichard A (2012). Deconstructing host-pathogen interactions in Drosophila. Dis. Model. Mech 5, 48–61. 10.1242/dmm.000406. [PubMed: 21979942]
18. Schneider J, and Imler JL (2021). Sensing and signalling viral infection in drosophila. Dev. Comp. Immunol 117, 103985. 10.1016/j.dci.2020.103985. [PubMed: 33358662]
19. Harnish JM, Link N, and Yamamoto S (2021). Drosophila as a Model for Infectious Diseases. Int. J. Mol. Sci 22, 2724. 10.3390/ijms22052724. [PubMed: 33800390]
20. Zhu JY, Lee JG, van de Leemput J, Lee H, and Han Z (2021). Functional analysis of SARS-CoV-2 proteins in Drosophila identifies Orf6-induced pathogenic effects with Selinexor as an effective treatment. Cell Biosci 11, 59. 10.1186/s13578-021-00567-8. [PubMed: 33766136]
21. van de Leemput J, and Han Z (2021). Drosophila, a powerful model to study virus-host interactions and pathogenicity in the fight against SARS-CoV-2. Cell Biosci 11, 110. 10.1186/s13578-021-00621-5. [PubMed: 34120640]
22. Nainu F, Rahmatika D, Emran TB, and Harapan H (2020). Potential Application of Drosophila melanogaster as a Model Organism in COVID-19-Related Research. Front. Pharmacol 11, 588561. 10.3389/fphar.2020.588561. [PubMed: 33013425]
23. Herrera P, and Cauchi RJ (2021). ACE and ACE2: insights from Drosophila and implications for COVID-19. Heliyon 7, e08555. 10.1016/j.heliyon.2021.e08555. [PubMed: 34901515]
24. Zhu JY, Wang G, Huang X, Lee H, Lee JG, Yang P, van de Leemput J, Huang W, Kane MA, Yang P, and Han Z (2022). SARS-CoV-2 Nsp6 damages Drosophila heart and mouse cardiomyocytes through MGA/MAX complex-mediated increased glycolysis. Commun. Biol 5, 1039. 10.1038/s42003-022-03986-6. [PubMed: 36180527]

25. Kanca O, Zirin J, Garcia-Marques J, Knight SM, Yang-Zhou D, Amador G, Chung H, Zuo Z, Ma L, He Y, et al. (2019). An efficient CRISPR-based strategy to insert small and large fragments of DNA using short homology arms. Elife 8, e51539. 10.7554/eLife.51539. [PubMed: 31674908]
26. Kanca O, Zirin J, Hu Y, Tepe B, Dutta D, Lin WW, Ma L, Ge M, Zuo Z, Liu LP, et al. (2022). An expanded toolkit for Drosophila gene tagging using synthesized homology donor constructs for CRISPR-mediated homologous recombination. Elife 11, e76077. 10.7554/eLife.76077. [PubMed: 35723254]
27. Lee PT, Zirin J, Kanca O, Lin WW, Schulze KL, Li-Kroeger D, Tao R, Devereaux C, Hu Y, Chung V, et al. (2018). A gene-specific T2A-GAL4 library for Drosophila. Elife 7, e35574. 10.7554/eLife.35574. [PubMed: 29565247]
28. Kim DK, Knapp JJ, Kuang D, Chawla A, Cassonnet P, Lee H, Sheykhkarimli D, Samavarchi-Tehrani P, Abdouni H, Rayhan A, et al. (2020). A Comprehensive, Flexible Collection of SARS-CoV-2 Coding Regions. G3 (Bethesda) 10, 3399–3402. 10.1534/g3.120.401554. [PubMed: 32763951]
29. Brand AH, and Perrimon N (1993). Targeted gene expression as a means of altering cell fates and generating dominant phenotypes. Development 118, 401–415. [PubMed: 8223268]
30. Wu F, Zhao S, Yu B, Chen Y-M, Wang W, Song Z-G, Hu Y, Tao Z-W, Tian J-H, Pei Y-Y, et al. (2020). A new coronavirus associated with human respiratory disease in China. Nature 579, 265–269. 10.1038/s41586-020-2008-3. [PubMed: 32015508]
31. Bischof J, Björklund M, Furger E, Schertel C, Taipale J, and Basler K (2013). A versatile platform for creating a comprehensive UASORFeome library in Drosophila. Development 140, 2434–2442. 10.1242/dev.088757. [PubMed: 23637332]
32. Kanca O, Bellen HJ, and Schnorrer F (2017). Gene Tagging Strategies To Assess Protein Expression, Localization, and Function in Drosophila. Genetics 207, 389–412. 10.1534/genetics.117.199968. [PubMed: 28978772]
33. Venken KJT, He Y, Hoskins RA, and Bellen HJ (2006). P[acman]: a BAC transgenic platform for targeted insertion of large DNA fragments in D. melanogaster. Science 314, 1747–1751. 10.1126/science.1134426. [PubMed: 17138868]
34. Hu Y, Flockhart I, Vinayagam A, Bergwitz C, Berger B, Perrimon N, and Mohr SE (2011). An integrative approach to ortholog prediction for disease-focused and other functional studies. BMC Bioinf 12, 357. 10.1186/1471-2105-12-357.
35. Nagarkar-Jaiswal S, Lee PT, Campbell ME, Chen K, Anguiano-Za-rate S, Gutierrez MC, Busby T, Lin WW, He Y, Schulze KL, et al. (2015). A library of MiMICs allows tagging of genes and reversible, spatial and temporal knockdown of proteins in Drosophila. Elife 4, e05338. 10.7554/eLife.05338. [PubMed: 25824290]
36. Venken KJT, Schulze KL, Haelterman NA, Pan H, He Y, Evans-Holm M, Carlson JW, Levis RW, Spradling AC, Hoskins RA, and Bellen HJ (2011). MiMIC: a highly versatile transposon insertion resource for engineering Drosophila melanogaster genes. Nat. Methods 8, 737–743. 10.1038/nmeth.1662. [PubMed: 21985007]
37. Diao F, Ironfield H, Luan H, Diao F, Shropshire WC, Ewer J, Marr E, Potter CJ, Landgraf M, and White BH (2015). Plug-and-play genetic access to drosophila cell types using exchangeable exon cassettes. Cell Rep 10, 1410–1421. 10.1016/j.celrep.2015.01.059. [PubMed: 25732830]
38. Barish S, Barakat TS, Michel BC, Mashtalir N, Phillips JB, Valencia AM, Ugur B, Wegner J, Scott TM, Bostwick B, et al. (2020). BICRA, a SWI/SNF Complex Member, Is Associated with BAF-Disorder Related Phenotypes in Humans and Model Organisms. Am. J. Hum. Genet 107, 1096–1112. 10.1016/j.ajhg.2020.11.003. [PubMed: 33232675]
39. Ansar M, Chung H-L, Al-Otaibi A, Elagabani MN, Ravenscroft TA, Paracha SA, Scholz R, Abdel Magid T, Sarwar MT, Shah SF, et al. (2019). Bi-allelic Variants in IQSEC1 Cause Intellectual Disability, Developmental Delay, and Short Stature. Am. J. Hum. Genet 105, 907–920. 10.1016/j.ajhg.2019.09.013. [PubMed: 31607425]
40. Wang J, Rousseau J, Kim E, Ehresmann S, Cheng YT, Duraine L, Zuo Z, Park YJ, Li-Kroeger D, Bi W, et al. (2019). Loss of Oxidation Resistance 1, OXR1, Is Associated with an Autosomal-Recessive Neurological Disease with Cerebellar Atrophy and Lysosomal Dysfunction. Am. J. Hum. Genet 105, 1237–1253. 10.1016/j.ajhg.2019.11.002. [PubMed: 31785787]

41. Dutta D, Briere LC, Kanca O, Marcogliese PC, Walker MA, High FA, Vanderver A, Krier J, Carmichael N, Callahan C, et al. (2020). De novo mutations in TOMM70, a receptor of the mitochondrial import translocase, cause neurological impairment. Hum. Mol. Genet 29, 1568–1579. 10.1093/hmg/ddaa081. [PubMed: 32356556]

42. Chung HL, Mao X, Wang H, Park YJ, Marcogliese PC, Rosenfeld JA, Burrage LC, Liu P, Murdock DR, Yamamoto S, et al. (2020). De Novo Variants in CDK19 Are Associated with a Syndrome Involving Intellectual Disability and Epileptic Encephalopathy. Am. J. Hum. Genet 106, 717–725. 10.1016/j.ajhg.2020.04.001. [PubMed: 32330417]

43. Wang L, Lin G, Zuo Z, Li Y, Byeon SK, Pandey A, and Bellen HJ (2022). Neuronal activity induces glucosylceramide that is secreted via exosomes for lysosomal degradation in glia. Sci. Adv 8, eabn3326. 10.1126/sciadv.abn3326.

44. Lu S, Hernan R, Marcogliese PC, Huang Y, Gertler TS, Akcaboy M, Liu S, Chung HL, Pan X, Sun X, et al. (2022). Loss-of-function variants in TIAM1 are associated with developmental delay, intellectual disability, and seizures. Am. J. Hum. Genet 109, 571–586. 10.1016/j.ajhg.2022.01.020. [PubMed: 35240055]

45. Lu S, Ma M, Mao X, Bacino CA, Jankovic J, Sutton VR, Bartley JA, Wang X, Rosenfeld JA, Beleza-Meireles A, et al. (2022). De novo variants in FRMD5 are associated with developmental delay, intellectual disability, ataxia, and abnormalities of eye movement. Am. J. Hum. Genet 109, 1932–1943. 10.1016/j.ajhg.2022.09.005. [PubMed: 36206744]

46. Bellen HJ, Wangler MF, and Yamamoto S (2019). The fruit fly at the interface of diagnosis and pathogenic mechanisms of rare and common human diseases. Hum. Mol. Genet 28, R207–R214. 10.1093/hmg/ddz135. [PubMed: 31227826]

47. Baldridge D, Wangler MF, Bowman AN, Yamamoto S, Undiagnosed Diseases Network; Schedl T, Pak SC, Postlethwait JH, Shin J, Solnica-Krezel L, et al. (2021). Model organisms contribute to diagnosis and discovery in the undiagnosed diseases network: current state and a future vision. Orphanet J. Rare Dis 16, 206. 10.1186/s13023-021-01839-9. [PubMed: 33962631]

48. Maiese A, Manetti AC, Bosetti C, Del Duca F, La Russa R, Frati P, Di Paolo M, Turillazzi E, and Fineschi V (2021). SARS-CoV-2 and the brain: A review of the current knowledge on neuropathology in COVID-19. Brain Pathol 31, e13013. 10.1111/bpa.13013. [PubMed: 34390282]

49. Maury A, Lyoubi A, Peiffer-Smadja N, de Broucker T, and Meppiel E (2021). Neurological manifestations associated with SARS-CoV-2 and other coronaviruses: A narrative review for clinicians. Rev. Neurol 177, 51–64. 10.1016/j.neurol.2020.10.001. [PubMed: 33446327]

50. Tao K, Tzou PL, Nouhin J, Gupta RK, de Oliveira T, Kosakovsky Pond SL, Fera D, and Shafer RW (2021). The biological and clinical significance of emerging SARS-CoV-2 variants. Nat. Rev. Genet 22, 757–773. 10.1038/s41576-021-00408-x. [PubMed: 34535792]

51. Bianchi M, Borsetti A, Ciccozzi M, and Pascarella S (2021). SARS-Cov-2 ORF3a: Mutability and function. Int. J. Biol. Macromol 170, 820–826. 10.1016/j.ijbiomac.2020.12.142. [PubMed: 33359807]

52. Issa E, Merhi G, Panossian B, Salloum T, and Tokajian S (2020). SARS-CoV-2 and ORF3a: Nonsynonymous Mutations, Functional Domains, and Viral Pathogenesis. mSystems 5, e00266–20. 10.1128/mSystems.00266-20. [PubMed: 32371472]

53. Ren Y, Shu T, Wu D, Mu J, Wang C, Huang M, Han Y, Zhang XY, Zhou W, Qiu Y, and Zhou X (2020). The ORF3a protein of SARS-CoV-2 induces apoptosis in cells. Cell. Mol. Immunol 17, 881–883. 10.1038/s41423-020-0485-9. [PubMed: 32555321]

54. Scott C, and Griffin S (2015). Viroporins: structure, function and potential as antiviral targets. J. Gen. Virol 96, 2000–2027. 10.1099/vir.0.000201. [PubMed: 26023149]

55. Wong SLA, Chen Y, Chan CM, Chan CSM, Chan PKS, Chui YL, Fung KP, Waye MMY, Tsui SKW, and Chan HYE (2005). In vivo functional characterization of the SARS-Coronavirus 3a protein in Drosophila. Biochem. Biophys. Res. Commun 337, 720–729. 10.1016/j.bbrc.2005.09.098. [PubMed: 16212942]

56. Majumdar P, and Niyogi S (2020). ORF3a mutation associated with higher mortality rate in SARS-CoV-2 infection. Epidemiol. Infect 148, e262. 10.1017/S0950268820002599. [PubMed: 33100263]

57. Wang R, Chen J, Gao K, Hozumi Y, Yin C, and Wei GW (2021). Analysis of SARS-CoV-2 mutations in the United States suggests presence of four substrains and novel variants. Commun. Biol 4, 228. 10.1038/s42003-021-01754-6. [PubMed: 33589648]
58. Zhang J, Li Q, Cruz Cosme RS, Gerzanich V, Tang Q, Simard JM, and Zhao RY (2021). Genome-Wide Characterization of SARS-CoV-2 Cytopathogenic Proteins in the Search of Antiviral Targets. mBio 13, e0016922. 10.1128/mbio.00169-22. [PubMed: 35164548]
59. Bier E (2005). Drosophila, the golden bug, emerges as a tool for human genetics. Nat. Rev. Genet 6, 9–23. 10.1038/nrg1503. [PubMed: 15630418]
60. Guichard A, McGillivray SM, Cruz-Moreno B, van Sorge NM, Nizet V, and Bier E (2010). Anthrax toxins cooperatively inhibit endocytic recycling by the Rab11/Sec15 exocyst. Nature 467, 854–858. 10.1038/nature09446. [PubMed: 20944747]
61. Schwartz R, Guichard A, Franc NC, Roy S, and Bier E (2020). A Drosophila Model for Clostridium difficile Toxin CDT Reveals Interactions with Multiple Effector Pathways. iScience 23, 100865. 10.1016/j.isci.2020.100865. [PubMed: 32058973]
62. Guichard A, Biehs B, Sturtevant MA, Wickline L, Chacko J, Howard K, and Bier E (1999). *rhomboid* and *Star* interact synergistically to promote EGFR/MAPK signaling during *Drosophila* wing vein development. Development 126, 2663–2676. [PubMed: 10331978]
63. Guichard A, Srinivasan S, Zimm G, and Bier E (2002). A screen for dominant mutations applied to components in the *Drosophila* EGF-R pathway. Proc. Natl. Acad. Sci. USA 99, 3752–3757. [PubMed: 11904431]
64. Segal D, and Gelbart WM (1985). Shortvein, a new component of the decapentaplegic gene complex in Drosophila melanogaster. Genetics 109, 119–143. 10.1093/genetics/109.1.119. [PubMed: 3917963]
65. Yu K, Srinivasan S, Shimmi O, Biehs B, Rashka KE, Kimelman D, O'Connor MB, and Bier E (2000). Processing of the Drosophila Sog protein creates a novel BMP inhibitory activity. Development 127, 2143–2154. 10.1242/dev.127.10.2143. [PubMed: 10769238]
66. Biehs B, Sturtevant MA, and Bier E (1998). Boundaries in the *Drosophila* wing imaginal disc organize vein-specific genetic programs. Development 125, 4245–4257. [PubMed: 9753679]
67. Crozatier M, Glise B, and Vincent A (2002). Connecting Hh, Dpp and EGF signalling in patterning of the *Drosophila* wing; the pivotal role of *collier/knot* in the AP organiser. Development 129, 4261–4269. [PubMed: 12183378]
68. Sturtevant MA, and Bier E (1995). Analysis of the genetic hierarchy guiding wing vein development in *Drosophila*. Development 121, 785–801. [PubMed: 7720583]
69. Capdevila J, and Guerrero I (1994). Targeted expression of the signaling molecule decapentaplegic induces pattern duplications and growth alterations in Drosophila wings. EMBO J 13, 4459–4468. 10.1002/j.1460-2075.1994.tb06768.x. [PubMed: 7925288]
70. Brentrup D, Lerch H, Jäckle H, and Noll M (2000). Regulation of *Drosophila* wing vein patterning: *net* encodes a bHLH protein repressing *rhomboid* and is repressed by *rhomboid*-dependent Egfr signalling. Development 127, 4729–4741. [PubMed: 11023875]
71. Matakatsu H, Tadokoro R, Gamo S, and Hayashi S (1999). Repression of the wing vein development in Drosophila by the nuclear matrix protein plexus. Development 126, 5207–5216. [PubMed: 10556047]
72. Gabay L, Seger R, and Shilo BZ (1997). In situ activation pattern of Drosophila EGF receptor pathway during development. Science 277, 1103–1106. 10.1126/science.277.5329.1103. [PubMed: 9262480]
73. Tanimoto H, Itoh S, ten Dijke P, and Tabata T (2000). Hedgehog creates a gradient of DPP activity in Drosophila wing imaginal discs. Mol. Cell 5, 59–71. 10.1016/s1097-2765(00)80403-7. [PubMed: 10678169]
74. Guichard A, Park JM, Cruz-Moreno B, Karin M, and Bier E (2006). Anthrax lethal factor and edema factor act on conserved targets in Drosophila. Proc. Natl. Acad. Sci. USA 103, 3244–3249. 10.1073/pnas.0510748103. [PubMed: 16455799]
75. Kirchdoerfer RN, and Ward AB (2019). Structure of the SARS-CoV nsp12 polymerase bound to nsp7 and nsp8 co-factors. Nat. Commun 10, 2342. 10.1038/s41467-019-10280-3. [PubMed: 31138817]

76. Sutton G, Fry E, Carter L, Sainsbury S, Walter T, Nettleship J, Berrow N, Owens R, Gilbert R, Davidson A, et al. (2004). The nsp9 replicase protein of SARS-coronavirus, structure and functional insights. Structure 12, 341–353. 10.1016/j.str.2004.01.016. [PubMed: 14962394]
77. te Velthuis AJW, van den Worm SHE, and Snijder EJ (2012). The SARS-coronavirus nsp7+nsp8 complex is a unique multimeric RNA polymerase capable of both de novo initiation and primer extension. Nucleic Acids Res 40, 1737–1747. 10.1093/nar/gkr893. [PubMed: 22039154]
78. Zhai Y, Sun F, Li X, Pang H, Xu X, Bartlam M, and Rao Z (2005). Insights into SARS-CoV transcription and replication from the structure of the nsp7-nsp8 hexadecamer. Nat. Struct. Mol. Biol 12, 980–986. 10.1038/nsmb999. [PubMed: 16228002]
79. de Amorim J, Slavotinek A, Fasken MB, Corbett AH, and Morton DJ (2020). Modeling Pathogenic Variants in the RNA Exosome. RNA Dis 7, e1166. [PubMed: 34676290]
80. Van V, and Smith AT (2020). ATE1-Mediated Post-Translational Arginylation Is an Essential Regulator of Eukaryotic Cellular Homeostasis. ACS Chem. Biol 15, 3073–3085. 10.1021/acschembio.0c00677. [PubMed: 33228359]
81. Karakozova M, Kozak M, Wong CCL, Bailey AO, Yates JR 3rd, Mogilner A, Zebroski H, and Kashina A (2006). Arginylation of beta-actin regulates actin cytoskeleton and cell motility. Science 313, 192–196. 10.1126/science.1129344. [PubMed: 16794040]
82. Saha S, Mundia MM, Zhang F, Demers RW, Korobova F, Svitkina T, Perieteanu AA, Dawson JF, and Kashina A (2010). Arginylation regulates intracellular actin polymer level by modulating actin properties and binding of capping and severing proteins. Mol. Biol. Cell 21, 1350–1361. 10.1091/mbc.E09-09-0829. [PubMed: 20181827]
83. Swain J, Merida P, Rubio K, Bracquemond D, Aguilar-Ordoñez I, Günther S, Barreto G, and Muriaux D (2022). Reorganization of F-actin nanostructures is required for the late phases of SARS-CoV-2 replication in pulmonary cells. Preprint at bioRxiv 10.1101/2022.03.08.483451.
84. Pavlyk I, Leu NA, Vedula P, Kurosaka S, and Kashina A (2018). Rapid and dynamic arginylation of the leading edge beta-actin is required for cell migration. Traffic 19, 263–272. 10.1111/tra.12551. [PubMed: 29384244]
85. Saha S, Wang J, Buckley B, Wang Q, Lilly B, Chernov M, and Kashina A (2012). Small molecule inhibitors of arginyltransferase regulate arginylation-dependent protein degradation, cell motility, and angiogenesis. Biochem. Pharmacol 83, 866–873. 10.1016/j.bcp.2012.01.012. [PubMed: 22280815]
86. Macedo-Da-Silva J, Rosa-Fernandes L, Gomes VDM, Santiago VF, Santos DM, Molnar CMS, Barboza BR, De Souza EE, Marques RF, Boscardin SB, et al. (2023). Protein Arginylation Is Regulated during SARS-CoV-2 Infection. Viruses 15, 290. 10.3390/v15020290. [PubMed: 36851505]
87. Salgado-Benvindo C, Thaler M, Tas A, Ogando NS, Bredenbeek PJ, Ninaber DK, Wang Y, Hiemstra PS, Snijder EJ, and van Hemert MJ (2020). Suramin Inhibits SARS-CoV-2 Infection in Cell Culture by Interfering with Early Steps of the Replication Cycle. Antimicrob. Agents Chemother 64, e00900–20. 10.1128/AAC.00900-20. [PubMed: 32513797]
88. Shou S, Liu M, Yang Y, Kang N, Song Y, Tan D, Liu N, Wang F, Liu J, and Xie Y (2021). Animal Models for COVID-19: Hamsters, Mouse, Ferret, Mink, Tree Shrew, and Non-human Primates. Front. Microbiol 12, 626553. 10.3389/fmicb.2021.626553. [PubMed: 34531831]
89. Chung HL, Wangler MF, Marcogliese PC, Jo J, Ravenscroft TA, Zuo Z, Duraine L, Sadeghzadeh S, Li-Kroeger D, Schmidt RE, et al. (2020). Loss- or Gain-of-Function Mutations in ACOX1 Cause Axonal Loss via Different Mechanisms. Neuron 106, 589–606.e6. 10.1016/j.neuron.2020.02.021. [PubMed: 32169171]
90. Chung HL, Ye Q, Park YJ, Zuo Z, Mok JW, Kanca O, Tattikota SG, Lu S, Perrimon N, Lee HK, and Bellen HJ (2023). Very-long-chain fatty acids induce glial-derived sphingosine-1-phosphate synthesis, secretion, and neuroinflammation. Cell Metabol 35, 855–874.e5. 10.1016/j.cmet.2023.03.022.
91. Lin G, Lee PT, Chen K, Mao D, Tan KL, Zuo Z, Lin WW, Wang L, and Bellen HJ (2018). Phospholipase PLA2G6, a Parkinsonism-Associated Gene, Affects Vps26 and Vps35, Retromer Function, and Ceramide Levels, Similar to alpha-Synuclein Gain. Cell Metabol 28, 605–618.e6. 10.1016/j.cmet.2018.05.019.

92. Lin G, Tepe B, McGrane G, Tipon RC, Croft G, Panwala L, Hope A, Liang AJH, Zuo Z, Byeon SK, et al. (2023). Exploring therapeutic strategies for infantile neuronal axonal dystrophy (INAD/PARK14). Elife 12, e82555. 10.7554/eLife.82555. [PubMed: 36645408]

93. Beckman D, Bonillas A, Diniz GB, Ott S, Roh JW, Elizaldi SR, Schmidt BA, Sammak RL, Van Rompay KKA, Iyer SS, and Morrison JH (2022). SARS-CoV-2 infects neurons and induces neuroinflammation in a non-human primate model of COVID-19. Cell Rep 41, 111573. 10.1016/j.celrep.2022.111573. [PubMed: 36288725]

94. Shanley JE, Valenciano AF, Timmons G, Miner AE, Kakarla V, Rempe T, Yang JH, Gooding A, Norman MA, Banks SJ, et al. (2022). Longitudinal evaluation of neurologic-post acute sequelae SARS-CoV-2 infection symptoms. Ann. Clin. Transl. Neurol 9, 995–1010. 10.1002/acn3.51578. [PubMed: 35702954]

95. Stefanou MI, Palaiodimou L, Bakola E, Smyrnis N, Papadopoulou M, Paraskevas GP, Rizos E, Boutati E, Grigoriadis N, Krogias C, et al. (2022). Neurological manifestations of long-COVID syndrome: a narrative review. Ther. Adv. Chronic Dis 13, 20406223221076890. 10.1177/20406223221076890.

96. Deal SL, and Yamamoto S (2018). Unraveling Novel Mechanisms of Neurodegeneration Through a Large-Scale Forward Genetic Screen in Drosophila. Front. Genet 9, 700. 10.3389/fgene.2018.00700. [PubMed: 30693015]

97. Yu K, Kang KH, Heine P, Pyati U, Srinivasan S, Biehs B, Kimelman D, and Bier E (2004). Cysteine repeat domains and adjacent sequences determine distinct bone morphogenetic protein modulatory activities of the Drosophila Sog protein. Genetics 166, 1323–1336. 10.1534/genetics.166.3.1323. [PubMed: 15082551]

98. Wang CY, Lu CY, Li SW, Lai CC, Hua CH, Huang SH, Lin YJ, Hour MJ, and Lin CW (2017). SARS coronavirus papain-like protease up-regulates the collagen expression through non-Samd TGF-beta1 signaling. Virus Res 235, 58–66. 10.1016/j.virusres.2017.04.008. [PubMed: 28414040]

99. Zhao X, Nicholls JM, and Chen YG (2008). Severe acute respiratory syndrome-associated coronavirus nucleocapsid protein interacts with Smad3 and modulates transforming growth factor-beta signaling. J. Biol. Chem 283, 3272–3280. 10.1074/jbc.M708033200. [PubMed: 18055455]

100. Chatterjee B, and Thakur SS (2022). SARS-CoV-2 Infection Triggers Phosphorylation: Potential Target for Anti-COVID-19 Therapeutics. Front. Immunol 13, 829474. 10.3389/fimmu.2022.829474. [PubMed: 35251015]

101. Vaz de Paula CB, Nagashima S, Liberalesso V, Collete M, da Silva FPG, Oricil AGG, Barbosa GS, da Silva GVC, Wiedmer DB, da Silva Dezidério F, and Noronha L (2021). COVID-19: Immunohisto-chemical Analysis of TGF-beta Signaling Pathways in Pulmonary Fibrosis. Int. J. Mol. Sci 23, 168. 10.3390/ijms23010168. [PubMed: 35008594]

102. Carlson FR Jr., Bosukonda D, Keck PC, and Carlson WD (2020). Multiorgan Damage in Patients With COVID-19: Is the TGF-beta/BMP Pathway the Missing Link? JACC. Basic Transl. Sci 5, 1145–1148. 10.1016/j.jacbts.2020.09.003. [PubMed: 32984657]

103. Chu DKW, Hui KPY, Gu H, Ko RLW, Krishnan P, Ng DYM, Liu GYZ, Wan CKC, Cheung MC, Ng KC, et al. (2021). Introduction of ORF3a-Q57H SARS-CoV-2 Variant Causing Fourth Epidemic Wave of COVID-19, Hong Kong, China. Emerg. Infect. Dis 27, 1492–1495. 10.3201/eid2705.210015. [PubMed: 33900193]

104. Xue L, Jing S, Zhang K, Milne R, and Wang H (2022). Infectivity versus fatality of SARS-CoV-2 mutations and influenza. Int. J. Infect. Dis 121, 195–202. 10.1016/j.ijid.2022.05.031.

105. Almasy KM, Davies JP, and Plate L (2021). Comparative Host Interactomes of the SARS-CoV-2 Nonstructural Protein 3 and Human Coronavirus Homologs. Mol. Cell. Proteomics 20, 100120. 10.1016/j.mcpro.2021.100120. [PubMed: 34186245]

106. Scott BM, Lacasse V, Blom DG, Tonner PD, and Blom NS (2022). Predicted coronavirus Nsp5 protease cleavage sites in the human proteome. BMC Genom. Data 23, 25. 10.1186/s12863-022-01044-y. [PubMed: 35379171]

107. Liu F, Chang L, and Hu J (2020). Activating transcription factor 6 regulated cell growth, migration and inhibiteds cell apoptosis and autophagy via MAPK pathway in cervical cancer. J. Reprod. Immunol 139, 103120. 10.1016/j.jri.2020.103120. [PubMed: 32234634]

108. Aleebrahim-Dehkordi E, Ghoshouni H, Koochaki P, Esmaili-Deh-kordi M, Aleebrahim E, Chichagi F, Jafari A, Hanaei S, Heidari-Soureshjani E, and Rezaei N (2023). Targeting the vital non-structural proteins (NSP12, NSP7, NSP8 and NSP3) from SARS-CoV-2 and inhibition of RNA polymerase by natural bioactive compound naringenin as a promising drug candidate against COVID-19. J. Mol. Struct 1287, 135642. 10.1016/j.molstruc.2023.135642. [PubMed: 37131962]

109. Peng Q, Peng R, Yuan B, Zhao J, Wang M, Wang X, Wang Q, Sun Y, Fan Z, Qi J, et al. (2020). Structural and Biochemical Characterization of the nsp12-nsp7-nsp8 Core Polymerase Complex from SARS-CoV-2. Cell Rep 31, 107774. 10.1016/j.celrep.2020.107774. [PubMed: 32531208]

110. Wu J, Chen Z, Han X, Chen Q, Wang Y, and Feng T (2023). SARS-CoV-2 RNA-dependent RNA polymerase as a target for high-throughput drug screening. Future Virol 18, 51–62. 10.2217/fvl-2021-0335.

111. Morton DJ, Kuiper EG, Jones SK, Leung SW, Corbett AH, and Fasken MB (2018). The RNA exosome and RNA exosome-linked disease. RNA 24, 127–142. 10.1261/rna.064626.117. [PubMed: 29093021]

112. Fasken MB, Morton DJ, Kuiper EG, Jones SK, Leung SW, and Corbett AH (2020). The RNA Exosome and Human Disease. Methods Mol. Biol 2062, 3–33. 10.1007/978-1-4939-9822-7_1. [PubMed: 31768969]

113. Moll T, Odon V, Harvey C, Collins MO, Peden A, Franklin J, Graves E, Marshall JN, Santos Souza C.d., Zhang S, et al. (2022). Low expression of EXOSC2 protects against clinical COVID-19 and impedes SARS-CoV-2 replication. Preprint at bioRxiv2022.03.06.483172 10.1101/2022.03.06.483172.

114. Ariumi Y (2022). Host Cellular RNA Helicases Regulate SARS-CoV-2 Infection. J. Virol 96, e0000222. 10.1128/jvi.00002-22. [PubMed: 35107372]

115. Squeglia F, Romano M, Ruggiero A, Maga G, and Berisio R (2020). Host DDX Helicases as Possible SARS-CoV-2 Proviral Factors: A Structural Overview of Their Hijacking Through Multiple Viral Proteins. Front. Chem 8, 602162. 10.3389/fchem.2020.602162. [PubMed: 33381492]

116. Bennett RL, Swaroop A, Troche C, and Licht JD (2017). The Role of Nuclear Receptor-Binding SET Domain Family Histone Lysine Methyltransferases in Cancer. Cold Spring Harb. Perspect. Med 7, a026708. 10.1101/cshperspect.a026708. [PubMed: 28193767]

117. Lian L, Suzuki A, Hayes V, Saha S, Han X, Xu T, Yates JR 3rd, Poncz M, Kashina A, and Abrams CS (2014). Loss of ATE1-mediated arginylation leads to impaired platelet myosin phosphorylation, clot retraction, and in vivo thrombosis formation. Haematologica 99, 554–560. 10.3324/haematol.2013.093047. [PubMed: 24293517]

118. Singh K, Gupta A, Sarkar A, Gupta I, Rana S, Sarkar S, and Khan S (2020). Arginyltransferase knockdown attenuates cardiac hypertrophy and fibrosis through TAK1-JNK1/2 pathway. Sci. Rep 10, 598. 10.1038/s41598-019-57379-7. [PubMed: 31953451]

119. Jiang C, Moorthy BT, Patel DM, Kumar A, Morgan WM, Alfonso B, Huang J, Lampidis TJ, Isom DG, Barrientos A, et al. (2020). Regulation of Mitochondrial Respiratory Chain Complex Levels, Organization, and Function by Arginyltransferase 1. Front. Cell Dev. Biol 8, 603688. 10.3389/fcell.2020.603688. [PubMed: 33409279]

120. Deka K, Singh A, Chakraborty S, Mukhopadhyay R, and Saha S (2016). Protein arginylation regulates cellular stress response by stabilizing HSP70 and HSP40 transcripts. Cell Death Dis 2, 16074. 10.1038/cddiscovery.2016.74.

121. Ji CH, Kim HY, Heo AJ, Lee SH, Lee MJ, Kim SB, Srinivasrao G, Mun SR, Cha-Molstad H, Ciechanover A, et al. (2019). The N-Degron Pathway Mediates ER-phagy. Mol. Cell 75, 1058–1072.e9. 10.1016/j.molcel.2019.06.028. [PubMed: 31375263]

122. Galiano MR, Goitea VE, and Hallak ME (2016). Post-translational protein arginylation in the normal nervous system and in neurodegeneration. J. Neurochem 138, 506–517. 10.1111/jnc.13708. [PubMed: 27318192]

123. Vedula P, Tang HY, Speicher DW, and Kashina A; UPenn COVID Processing Unit (2022). Protein Posttranslational Signatures Identified in COVID-19 Patient Plasma. Front. Cell Dev. Biol 10, 807149. 10.3389/fcell.2022.807149. [PubMed: 35223838]

124. MGC Project Team; Temple G, Gerhard DS, Rasooly R, Feingold EA, Good PJ, Robinson C, Mandich A, Derge JG, Lewis J, et al. (2009). The completion of the Mammalian Gene Collection (MGC). Genome Res 19, 2324–2333. 10.1101/gr.095976.109. [PubMed: 19767417]

125. Bischof J, Maeda RK, Hediger M, Karch F, and Basler K (2007). An optimized transgenesis system for Drosophila using germ-line-specific phiC31 integrases. Proc. Natl. Acad. Sci. USA 104, 3312–3317. 10.1073/pnas.0611511104. [PubMed: 17360644]

126. Markstein M, Pitsouli C, Villalta C, Celniker SE, and Perrimon N (2008). Exploiting position effects and the gypsy retrovirus insulator to engineer precisely expressed transgenes. Nat. Genet 40, 476–483. 10.1038/ng.101. [PubMed: 18311141]

127. Port F, and Bullock SL (2016). Augmenting CRISPR applications in Drosophila with tRNA-flanked sgRNAs. Nat. Methods 13, 852–854. 10.1038/nmeth.3972. [PubMed: 27595403]

128. Port F, Chen HM, Lee T, and Bullock SL (2014). Optimized CRISPR/Cas tools for efficient germline and somatic genome engineering in Drosophila. Proc. Natl. Acad. Sci. USA 111, E2967–E2976. 10.1073/pnas.1405500111. [PubMed: 25002478]

129. Kondo S, and Ueda R (2013). Highly improved gene targeting by germ-line-specific Cas9 expression in Drosophila. Genetics 195, 715–721. 10.1534/genetics.113.156737. [PubMed: 24002648]

130. Li-Kroeger D, Kanca O, Lee PT, Cowan S, Lee MT, Jaiswal M, Salazar JL, He Y, Zuo Z, and Bellen HJ (2018). An expanded toolkit for gene tagging based on MiMIC and scarless CRISPR tagging in Drosophila. Elife 7, e38709. 10.7554/eLife.38709. [PubMed: 30091705]

131. Goodman LD, Cope H, Nil Z, Ravenscroft TA, Charng WL, Lu S, Tien AC, Pfundt R, Koolen DA, Haaxma CA, et al. (2021). TNPO2 variants associate with human developmental delays, neurologic deficits, and dysmorphic features and alter TNPO2 activity in Drosophila. Am. J. Hum. Genet 108, 1669–1691. 10.1016/j.ajhg.2021.06.019. [PubMed: 34314705]

132. Lu SZ, Guo YS, Liang PZ, Zhang SZ, Yin S, Yin YQ, Wang XM, Ding F, Gu XS, and Zhou JW (2019). Suppression of astrocytic autophagy by alphaB-crystallin contributes to alpha-synuclein inclusion formation. Transl. Neurodegener 8, 3. 10.1186/s40035-018-0143-7. [PubMed: 30675347]

Highlights

- A *Drosophila* resource enables functional analysis of all SARS-Cov2 factors
- This collection allows expression of viral factors and human binding partners
- It also includes GAL4 insertions mutating fly orthologs of host binding partners
- NSP8 interacts with other viral factors and with the ATE1 arginyltransferase

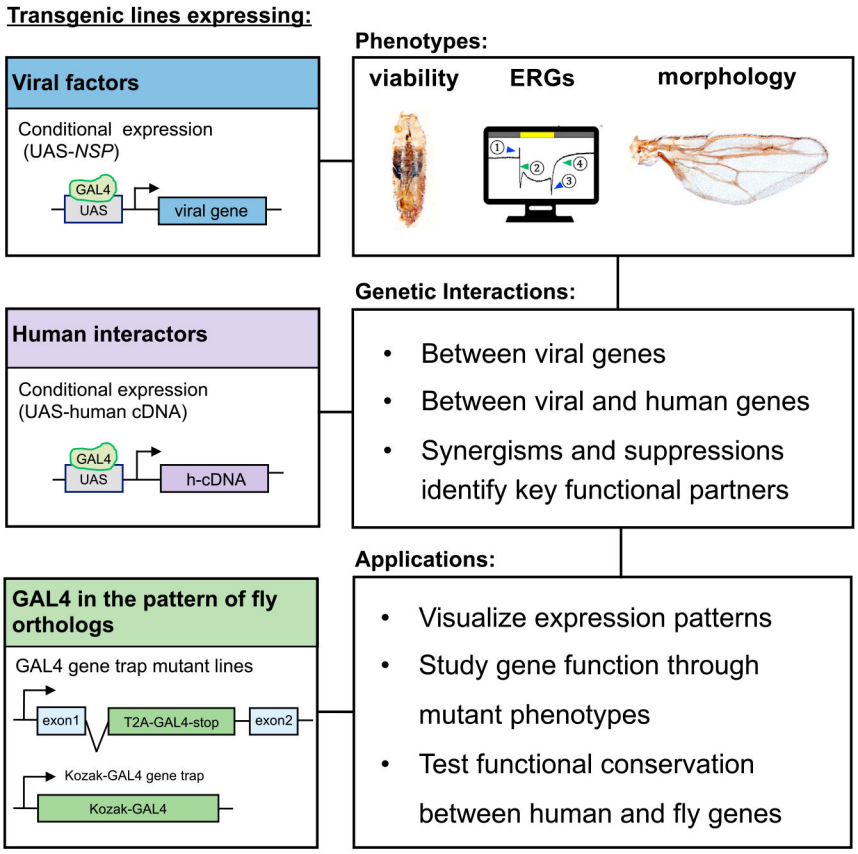

Figure 1. Functional analysis of SARS-CoV-2 factors in *Drosophila*

Three types of reagents were created for expression and functional analysis of SARS-CoV-2 factors and dedicated host interactors in *Drosophila* (left boxes): UAS lines expressing viral factors (top), UAS lines expressing their human binding partners (middle), and GAL4 gene trap lines allowing “humanization” for the fly homologs of these human genes (bottom). These reagents are used to produce specific phenotypes pertaining to lethality, wing and eye development, and neural function (top right). Phenotypes produced by viral factors can be used to probe for genetic interactions with human candidate genes (middle right). Results obtained from phenotypic and genetic analysis can be validated through further investigation: testing activity of selected pathways and testing co-expression of viral factor with RNAi of corresponding fly homologs. T2A-GAL4 and Kozak-GAL4 gene trap lines can be used to test functional conservation between fly and human orthologs and examining expression patterns of these fly genes (bottom right).

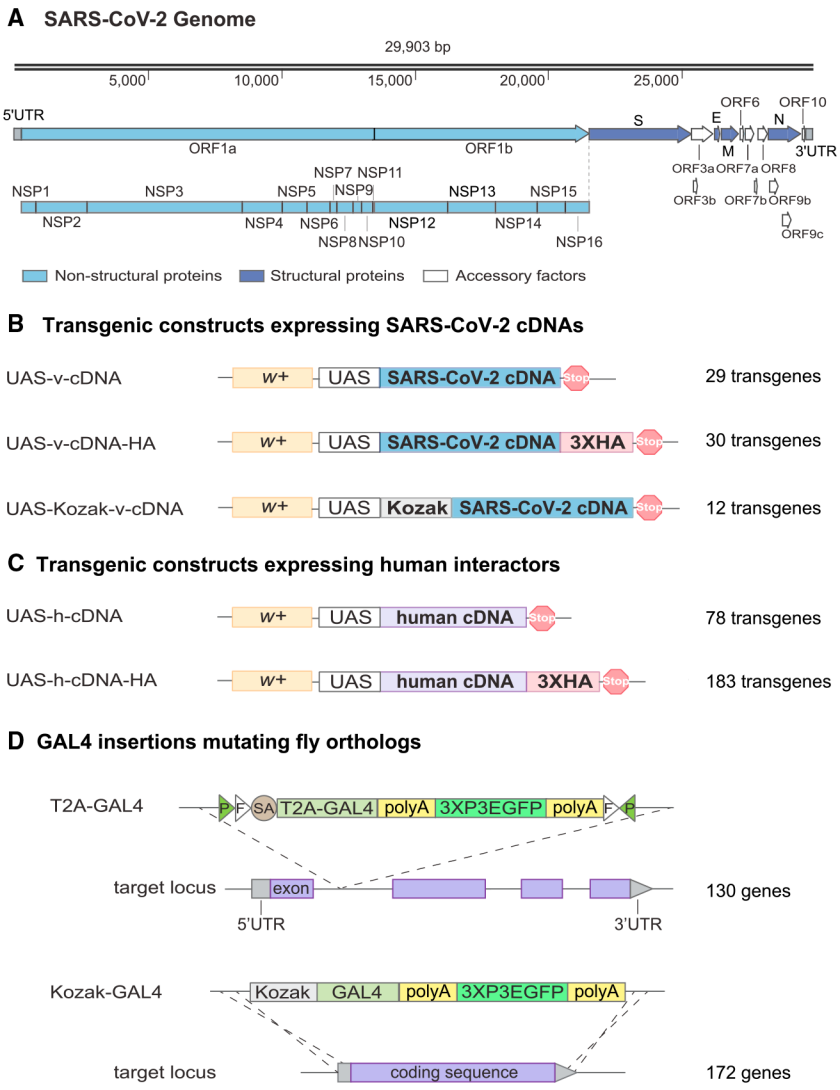

Figure 2. Generation of UAS-SARS-CoV-2, UAS-human-cDNA, and T2A-/Kozak-GAL4 stocks

(A) Genome organization of SARS-CoV-2. The viral genome encodes 29 proteins, including 16 non-structural proteins, four structural proteins, and nine accessory factors.

(B) Structure of UAS-SARS-CoV-2 transgenes. Each transgene was inserted into the same genomic site using φC31-mediated insertion. The total number of transgenes is indicated. "*W*+" indicates the mini-*white* genetic marker.

(C) Structure of transgenes expressing human interactors. UAS-human cDNAs were generated either with a native stop codon or with a C-terminal 33HA tag. "*W*+" indicates the mini-*white* marker.

(D) Strategies to generate T2A-GAL4 and Kozak-GAL4 alleles using CRISPR-mediated homologous recombination. The T2A-GAL4 cassette is inserted into a suitable coding intron (intron flanked by two coding exons) of the target locus. The Kozak-GAL4 cassette replaces the coding sequence when no suitable introns are present. P, attP; F, FRT; SA, splice acceptor.

A **Lethality phenotypes from ubiquitous expression of SARS-CoV2 factors**

SARS-CoV-2 UAS-cDNA	*Ubiquitous GAL4*					
	Tub		*Act*		*da*	
	no tag	HA tag	no tag	HA tag	no tag	HA tag
NSP1	lethal	lethal	lethal	lethal	lethal	lethal
NSP2	viable	viable	viable	semi-lethal	viable	viable
NSP3	lethal	lethal	lethal	viable	lethal	lethal
NSP4	viable	lethal	viable	lethal	viable	semi-lethal
NSP5	lethal	lethal	lethal	lethal	lethal	lethal
NSP6	lethal	lethal	viable	lethal	viable	lethal
NSP7	viable	viable	viable	viable	viable	viable
NSP8	viable	viable	viable	viable	viable	viable
NSP9	viable	viable	viable	viable	viable	viable
NSP10	viable	viable	viable	viable	viable	viable
NSP11	viable	viable	viable	viable	viable	viable
NSP12	viable	lethal	viable	semi-lethal	viable	semi-lethal
NSP13	lethal	viable	lethal	lethal	lethal	lethal
NSP14	lethal	viable	viable	viable	lethal	viable
NSP15	lethal	lethal	semi-lethal	lethal	lethal	lethal
NSP16	viable	viable	viable	viable	viable	viable
S	viable	lethal	viable	lethal	viable	lethal
E	lethal	lethal	viable	viable	semi-lethal	viable
M	semi-lethal	lethal	semi-lethal	lethal	viable	lethal
N	viable	semi-lethal	viable	viable	viable	semi-lethal
ORF3a	lethal	lethal	semi-lethal	lethal	lethal	lethal
ORF3b	viable	lethal	viable	lethal	viable	lethal
ORF6	lethal	lethal	lethal	lethal	semi-lethal	lethal
ORF7a	semi-lethal	lethal	viable	semi-lethal	semi-lethal	lethal
ORF7b	semi-lethal	lethal	viable	lethal	viable	lethal
ORF8	viable	semi-lethal	viable	viable	viable	viable
ORF9b	viable	viable	viable	viable	viable	viable
ORF9c	viable	viable	viable	viable	viable	viable
ORF10	viable	lethal	viable	lethal	viable	semi-lethal

B **Summary of lethality phenotypes**

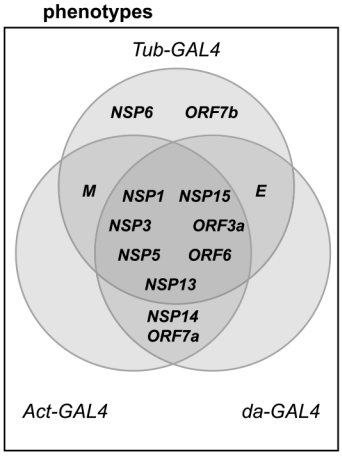

C **Phenotype severity of HA-tagged versus untagged SARS-CoV-2 factors**

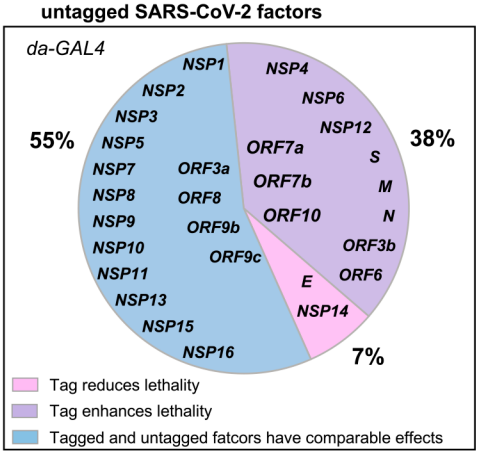

Figure 3. Functional evaluation of SARS-CoV-2 cDNAs through ubiquitous expression

(A) Lethality phenotypes resulting from overexpression of UAS-SARS-CoV-2 and UAS-SARS-CoV-2-HA transgenes driven by ubiquitous GAL4s (Tub-GAL4, Act-GAL4 and da-GAL4).

(B) Venn diagram summarizing lethality based on ubiquitous overexpression of SARS-CoV-2 transgenes.

(C) Severity of lethal phenotypes caused by UAS-SARS-CoV-2 and UAS-SARS-CoV-2-HA ubiquitous overexpression. Adding the HA tag tends to cause more severe phenotypes.

For (A) to (C), the flies were raised at 29°C.

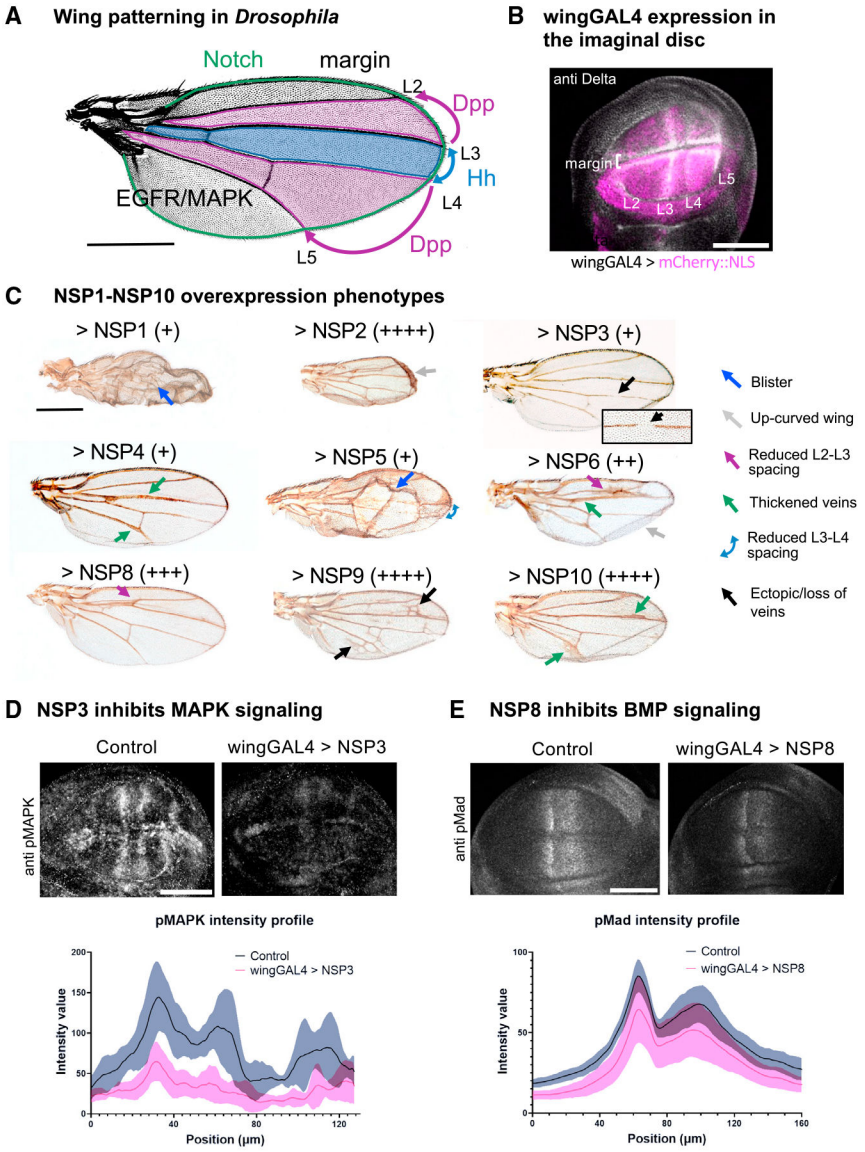

Figure 4. NSP1–10 cause specific wing phenotypes

(A) A wild-type wing with key signaling pathways and their roles in patterning during development. Hedgehog signaling (Hh, light blue) defines the distance between central veins L3 and L4. Dpp signaling (purple) defines the positioning of outer veins L2–L5. Notch signaling (green) defines vein thickness and margin fate. EGFR/MAPK signaling (black) controls cell proliferation/survival and vein fate. Scale bar represents 500 µm.

(B) A wild-type wing disc (the larval wing primordium) expressing mCherryNLS (magenta) driven by a strong dorsal-wing-specific GAL4 (MS1096 referred to as wingGAL4) and stained with an anti-Delta antibody (white). The Notch ligand Delta marks the position of the margin and longitudinal veins L3–L5. Scale bar represents 100 µm.

(C) Specific wing phenotypes caused by UAS-Kozak-NSP1–10 expressed under the control of wingGAL4 driver. Four expression levels were defined by different conditions to obtain viable and visible phenotypes: low expression (+, tubulinGAL80ts lowers expression to

obtain viable males at 25°C), moderate expression (++, females raised at 18°C), high expression (+++, males raised at 25°C), and very high expression (++++, two copies of the UAS transgene in individuals raised at room temperature). Colored arrows point to specific phenotype features in relation to the signaling pathways depicted in (A). Indigo arrows indicate blisters reflective of cell adhesion defects; gray arrows point to curved wings indicating cell proliferation/survival defects. Scale bar represents 500 μm.

(D) Imaginal discs stained with an anti-activated MAPK antibody (pMAPK). Elevated pMAPK marks the margin primordium and veins L3–L5 in a wild-type disc (left). In an NSP3-expressing disc (right), pMAPK staining is reduced, as predicted by the loss-of-vein phenotype in (C). Lower panel shows a pMAPK intensity profile for four discs of each genotype: NSP3-expressing discs show consistently lower pMAPK levels.

(E) Imaginal discs stained with an anti-phosphorylated Mad antibody (pMad), which reflects activation of Dpp signaling. pMad signal is elevated in a central zone between L2 and L5 vein primordia. In an NSP8-expressing disc (right), pMad staining is greatly reduced. Lower panel shows a pMad intensity profile for four discs of each genotype: NSP8-expressing discs show consistently lower pMad levels, as predicted by the adult wing phenotype in (C). Scale bars in (B), (D), and (E) represent 100 μm.

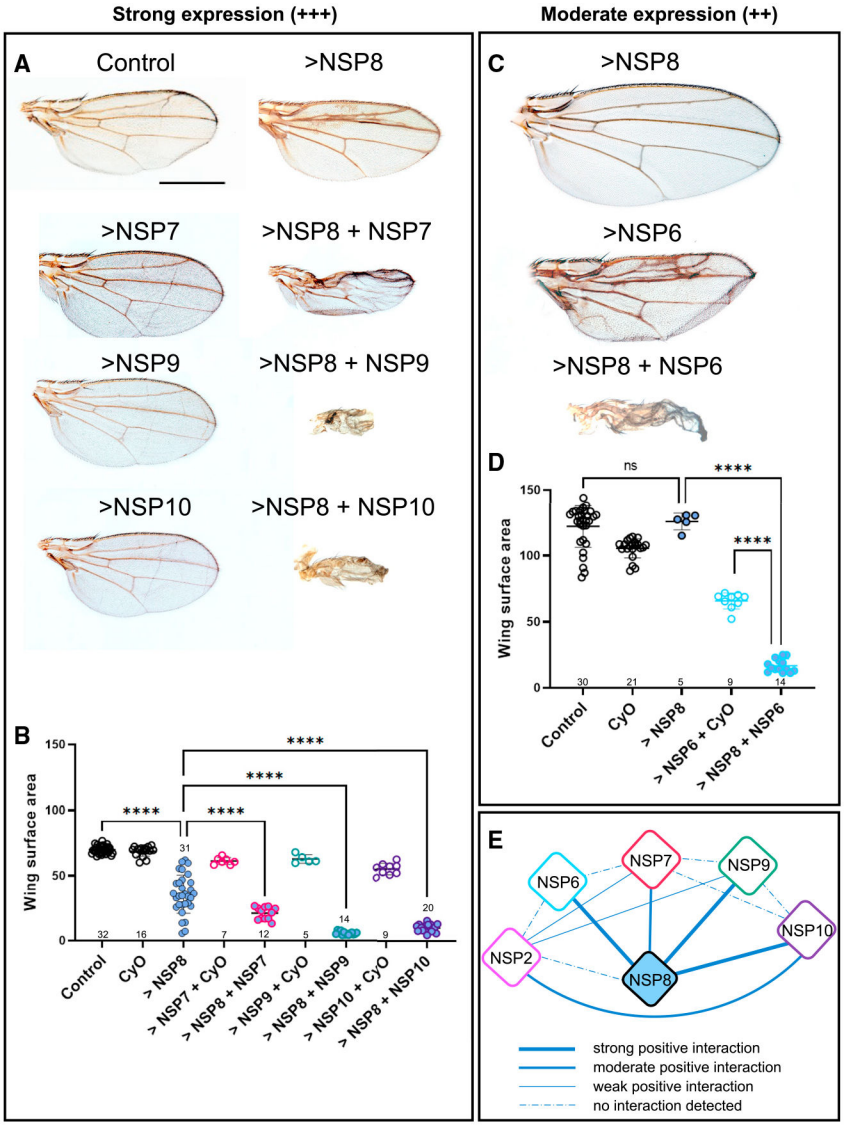

Figure 5. NSP8 interacts with NSP6, NSP7, NSP9, and NSP10

(A) Wing phenotypes from male flies of the indicated genotypes raised at 25°C. Under these conditions, NSP7, NSP9, and NSP10 do not produce any phenotype (wingGAL4>NSP in a CyO background, left panels). For flies co-expressing NSP8 + NSP7, NSP8 + NSP9, and NSP8 + NSP10, clear synergistic phenotypes are shown on right panels.

(B) Graph showing wing area quantifications of the genotypes shown in (A), with significant reduction in wing size when factors are expressed in pairwise combinations. Number of biological replicates is indicated. ****$p < 0.0001$.

(C) Wing phenotypes from wingGAL4>NSP8, wingGAL4>NSP6, and wingGAL4>NSP6 + NSP8 females raised at 18°C, showing synergism between NSP6 and NSP8.

(D) Graph showing wing area quantifications of genotypes shown in (C), with significant reduction in wing size when both factors are expressed. Number of biological replicates is indicated. ****$p < 0.0001$; ns, not significant.

(E) Summary diagram of genetic interactions found between NSP factors. NSP2 and NSP6–10 were tested in these co-expression experiments, but not NSP1 and NSP3–5, which require tubGAL80ts to obtain viable phenotypes. NSP8 displays strong or moderate positive interactions with NSP6, NSP7, NSP9, and NSP10, while other factors show no or weak interactions.

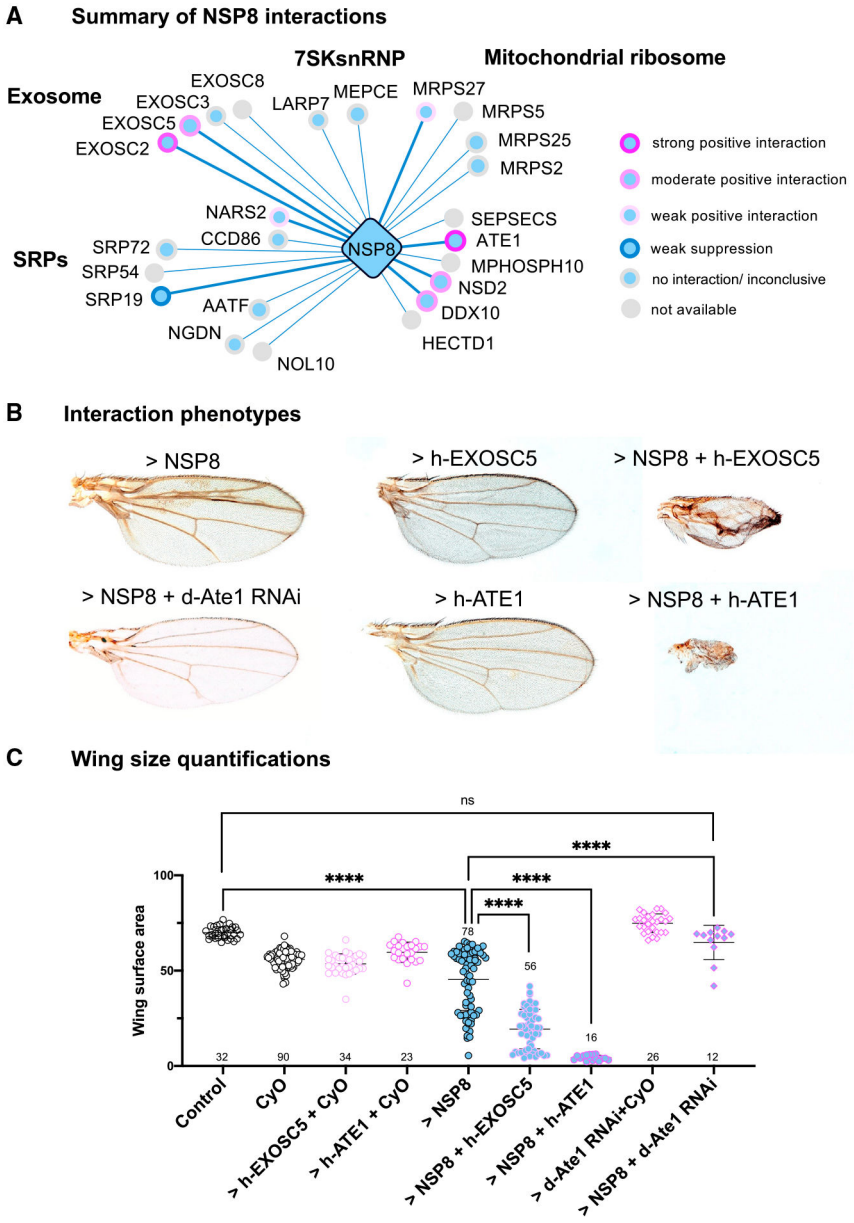

Figure 6. NSP8 interacts functionally with a set of human candidate genes

(A) Diagram summarizing the results from co-expression experiments involving NSP8 and individual human candidate cDNAs. The activity of the human cDNA alone was also assessed (in wing-GAL4>h-cDNA; CyO flies). Strong genetic interactions are indicated with a dark-pink circle, moderate interactions with a pink circle, and weak interactions with a light-pink circle. Suppression of the NSP8 phenotype is indicated with a blue circle; no interaction is indicated with a gray circle.

(B) Examples of strong and moderate interaction phenotypes between NSP8 and human candidate genes ATE1 and EXOSC5 (right panels), which alone do not produce any phenotype (middle panels). The NSP8 phenotype is strongly suppressed by co-expression of an h-ATE1 RNAi, indicating that the NSP8 phenotype is mediated by endogenous d-Ate1 (left bottom panel).

(C) Graph showing wing area quantifications of the genotypes shown in (B), with significant reduction in wing size when NSP8 is co-expressed with human candidate gene ATE1 or EXOSC5. d-ATE1 RNAi alone does not produce any phenotype but significantly suppresses the NSP8 phenotype. Number of biological replicates is indicated. ****$p < 0.0001$; ns, not significant.

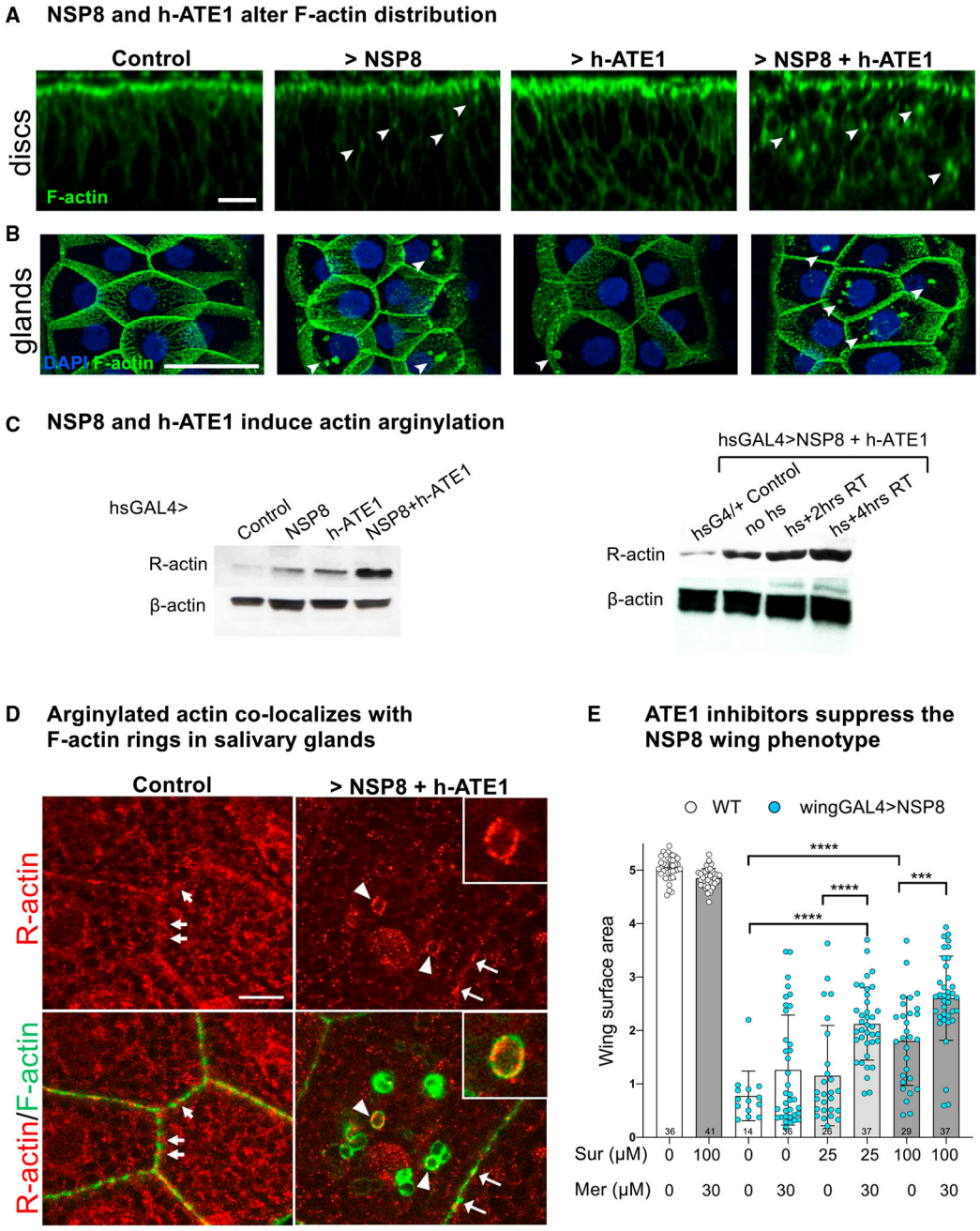

Figure 7. NSP8 cooperates with human ATE1 to deregulate actin dynamics and arginylation

(A) F-actin distribution in control, NSP8, ATE1, and NSP8 + ATE1-expressing discs (using the wingGAL4 driver). The F-actin network is mildly deregulated in NSP8 (few F-actin accumulations, arrowheads) and ATE1 discs, but severely disorganized in discs co-expressing NSP8 and ATE1 (many F-actin accumulations, arrowheads). Scale bars represent 10 μm.

(B) In salivary glands, expression of NSP8 or ATE1 alone or in combination results in formation of abnormal F-actin structures (arrowheads). The wingGAL4 driver used here is also expressed in salivary glands. Scale bars represent 100 μm.

(C) Western blot analysis of actin arginylation, using an anti-arginylated β-actin (R-actin) antibody. Control (hsGAL4/+), hsGAL4>NSP8, hsGAL4>ATE1, and hsGAL4>NSP8 + ATE1 adult flies were heat shocked for 90 min and proteins were extracted after a 3 h 30 min at room temperature. Actin arginylation is increased by NSP8 and ATE1 alone and cooperatively by both factors. Total levels of β-actin are not altered by expression of either factor (bottom). Actin arginylation following NSP8 and ATE1 co-expression increases over time after heat shock (right).

(D) *In situ* detection of actin arginylation in salivary glands. In control tissues (wingGAL4/+, left panels), R-actin (red) appears as a dotted ubiquitous stain mildly elevated at cell-cell junctions, which correlates with local interruptions (arrowheads) of the F-actin (green) network. Upon co-expression of NSP8 and ATE1 (wingGAL4>NSP8 + h-ATE1, bottom panels), R-actin co-localizes with F-actin at points of cortical accumulations (arrows) and some weaker staining F-actin rings (arrowheads). Scale bar represents 10 μm.

(E) Wing size quantifications of control (w1118; WT) and wingGAL4>NSP8 males (from wingGAL4; NSP8/CyO females crossed to w1118 males at 25°C) on different concentrations of suramin (Sur), with or without 30 μM merbromin (Mer). In absence of any drug, NSP8 produces a small wing phenotype in males. This phenotype is suppressed significantly in the presence of 100 μM suramin or 25 μM suramin + 30 μM merbromin. Addition of 30 μM merbromin also significantly ameliorates the NSP8 phenotypes obtained with 25 μM or 100 μM suramin. This suppressive effect is specific to NSP8-expressing wings, as the highest drug concentration (100 μM suramin + 30 μM merbromin) does not increase wing size in control w1118 animals but rather produces a small reduction in wing size. ***$p < 0.001$, ****$p < 0.0001$.

KEY RESOURCES TABLE

REAGENT or RESOURCE	SOURCE	IDENTIFIER
Antibodies		
Anti-Actin	Millipore	Cat # MAB1501; RRID:AB_2223041
Anti-NSP8	GeneTex	Cat #GTX632696; RRID:AB_2888329
Anti-NSP10	ABclonal	Cat # A20325
Anti pMAPK (197G2)	Cell Signaling	Cat # 4377; RRID: AB_331775
Anti pMad/pSmad	Cell Signaling	Cat #9516; RRID: AB_491015
Anti R-actin	Millipore	Cat #ABT264
Anti-β-actin	GeneTex	Cat #629630; RRID: AB_2728646
Alexa 647-Phalloidin	Thermo Fisher	Cat #222287
Mouse Anti HA	Millipore Sigma	Cat #11583816001; RRID:AB_514505
Goat anti-rabbit HRP	Jackson ImmunoResearch	Cat # 111-035-144; RRID: AB_2307391
Goat anti-mouse HRP	Jackson ImmunoResearch	Cat # 115-035-146; RRID: AB_2307392
Chemicals, peptides, and recombinant proteins		
Merbromin	Millipore Sigma	Cat#129-16-8
Suramin	Millipore Sigma	Cat#S2671
Critical commercial assays		
NEBuilder HiFi DNA Assembly	New England Biolabs	Cat#E5520
Experimental models: Organisms/strains		
D. melanogaster: Act-GAL4	BDSC	BDSC #3954
D. m: Tub-GAL4	BDSC	BDSC #5138
D. m: da-GAL4	BDSC	BDSC #55851
D. m: UAS-Empty	Goodman et al., 2021	N/A
D. m: UAS-ATE1	This work	BDSC #93215
D. m: Rh1-GAL4	BDSC	BDSC #8691
D. m: *Ate1*$^{CRMIC\text{-}TG4}$	This work	BDSC #81152
D. m: Ate1-Df	BDSC	BDSC #7896
D. m: Ate1-RNAi	BDSC	BDSC #53867
D. m: Ate1-RNAi	VDRC	VDRC #104360
D. m: MS1096-GAL4	BDSC	BDSC #8860
D. m: Heat Shock-GAL4	BDSC	BDSC #1799
D. m:vas-phiC31; VK33	BDSC and Kyoto Stock Center	BDSC #24871 KYOTO #130448
D. m:vas-phiC31; VK37	BDSC and Kyoto Stock Center	BDSC #24872 KYOTO #130449
Oligonucleotides		

REAGENT or RESOURCE	SOURCE	IDENTIFIER
UAS-NSP11 Forward: TTTTAAACGGGTTTGCGGTGTAAAACCCAGCTTTCTTGTACAA	This paper, Sigma	N/A
UAS-NSP11 Reverse: ACGATTGTGCATCAGCTGACATGGTGCCTGCIIIIIIGTACA	This paper, Sigma	N/A
UAS-NSP11-HA Forward: TTTTAAACGGGTTTGCGGTGAACCCAGCTTTCTTGTACAA	This paper, Sigma	N/A
UAS-NSP11-HA Reverse: ACGATTGTGCATCAGCTGACATGGTGCCTGCI IIIIIGTACA	This paper, Sigma	N/A
UAS-ORF3ap.Q57H-HA Forward: CCGTGTTCCATTCCGCCTCTAAGATCATC	This paper, Sigma	N/A
UAS-ORF3a p.Q57H-HA Reverse: CCAGCAGGGCCACACCCA	This paper, Sigma	N/A
Recombinant DNA		
pGW-HA.attB	Konrad Basler,(UZH)	GB: KC896838
pUASg-HA.attB	Konrad Basler,(UZH)	GB: KC896837
pUASg.attB	Konrad Basler,(UZH)	GB: EF362409.1
Software and algorithms		
ImageJ 1.53c	https://imagej.nih.gov/	N/A
Graphpad Prism 8	https://www.graphpad.com/	N/A
Microsoft Excel	Microsoft	N/A
Microsoft Powerpoint	Microsoft	N/A
Adobe Acrobat Pro	Adobe	N/A
Adobe Illustrator 2020	Adobe	N/A